The Astrophysical Journal, 891:73 (17pp), 2020 March 1 https://doi.org/10.3847/1538-4357/ab7375
© 2020. The American Astronomical Society. All rights reserved.

Prevalence of Complex Organic Molecules in Starless and Prestellar Cores within the Taurus Molecular Cloud

Samantha Scibelli and Yancy Shirley
Steward Observatory, University of Arizona, Tucson, AZ 85721, USA; sscibelli@email.arizona.edu
Received 2019 July 3; revised 2020 January 30; accepted 2020 February 5; published 2020 March 5

Abstract

The detection of complex organic molecules (COMs) toward dense, collapsing prestellar cores has sparked interest in the fields of astrochemistry and astrobiology, yet the mechanisms for COM formation are still debated. It was originally believed that COMs first form in ices, only to be irradiated by UV radiation from the surrounding interstellar radiation field as well as forming protostars, and subsequently photodesorbed into the gas phase. However, starless and prestellar cores do not have internal protostars to heat up and sublimate the ices. Alternative models using chemical energy have been developed to explain the desorption of COMs, yet in order to test these models, robust measurements of COM abundances are needed toward representative samples of cores. We have conducted a large sample survey of 31 starless and prestellar cores in the Taurus molecular cloud, detecting methanol (CH_3OH) in 100% of the cores targeted and acetaldehyde (CH_3CHO) in 70%. At least two transition lines of each molecule were measured, allowing us to place tight constraints on excitation temperature, column density, and abundance. Additional mapping of methanol revealed extended emission detected down to A_V as low as ∼3 mag. We find that COMs are detectable in the gas phase and are being formed early, at least hundreds of thousands of years prior to star and planet formation. The precursor molecule, CH_3OH, may be chemically linked to the more complex CH_3CHO; however, higher spatial resolution maps are needed to further test chemical models.

Unified Astronomy Thesaurus concepts: Astrochemistry (75); Star formation (1569); Dense interstellar clouds (371)

1. Introduction

Understanding the origin, production, and distribution of complex organic molecules (COMs) and prebiotic molecules is crucial for answering astrobiological questions about the origins of life. Amino acids and COMs important for the formation of life are found in laboratory studies of the energetic processing of interstellar ice analogs (i.e., Allamandola et al. 1988; Bernstein et al. 1995, 2002; Dworkin et al. 2001; Öberg et al. 2010; de Marcellus et al. 2011; Materese et al. 2013; Fedoseev et al. 2017; Modica et al. 2018; Nuevo et al. 2018; Dulieu et al. 2019). It is beyond the current capabilities of existing observatories to remotely study this predicted complexity in interstellar ices. However, observations of the gas-phase emission spectra of COMs provide a probe of the initial primitive stages of this important chemistry. A primary goal of the study of COMs is to understand where and how prebiotic molecules are formed in the interstellar medium prior to potential delivery to a planetary surface.

Before a low-mass ($M \leqslant$ few $M_\odot$) star is formed, it is conceived inside a dense clump of gas and dust known as a starless core. Dense starless cores and gravitationally bound prestellar cores are ideal regions to study the initial stages of chemistry prior to protostar and planet formation due to their simplicity: shallow temperature gradients, absence of an internal heat source, and absence of strong shocks or outflows (Benson & Myers 1989; Ward-Thompson et al. 1994; Evans et al. 2001; Bergin & Tafalla 2007; André et al. 2014). Studies of COMs directed toward starless cores are unique in that they probe one of the earliest phases in which COMs are observed in the interstellar medium. In a few cores, COMs have been detected in the gas phase from deep observations in the 3 mm band (e.g., Bacmann et al. 2012; Jiménez-Serra et al. 2016). We still do not know just how prevalent COMs are in this phase because observations have been limited to a few well-studied cores.

The formation of COMs at the cold (∼10 K) temperatures found in starless and prestellar cores is not well understood. Originally, COMs were believed to have been formed within icy dust grain mantles, where they would remain frozen through the prestellar phase, constructed at slow rates by UV radiation from nearby stars, the interstellar radiation field, and cosmic-ray impacts (e.g., Watanabe & Kouchi 2002; Chuang et al. 2017). They would then be released into the gas phase when heating from the forming protostar would sublimate the ice mantles driving a rich, warm gas-phase chemistry (Aikawa et al. 2008; Herbst & van Dishoeck 2009). This grain surface formation theory proved a better match to observations of COMs during protostellar phases, as pure gas-phase chemistry had been shown to lead to COM abundances several orders of magnitude lower than those observed (Charnley & Tielens 1992). Slow gas-phase rates of some key reactions have been confirmed by laboratory studies. For instance, a 3% yield of CH_3OH through the gas-phase dissociative recombination reaction of $CH_3OH_2^+$ is too inefficient to create sufficient amounts of interstellar gas-phase methanol (Geppert et al. 2006).

Since there is no protostar yet during the starless core phase, a major problem in explaining the observed gas-phase COM abundances lies in understanding how COMs or their precursors can be desorbed at cold temperatures. One possible solution is that the some COMs form in the gas phase from reactions with precursor radical molecules (i.e., HCO, CH_3O) that may themselves form in the grain ice mantles and are subsequently desorbed by the chemical energy released in their formation reactions (a process called reactive desorption). These radicals have been observed in the gas phase toward prestellar cores (Bacmann & Faure 2016). New models support

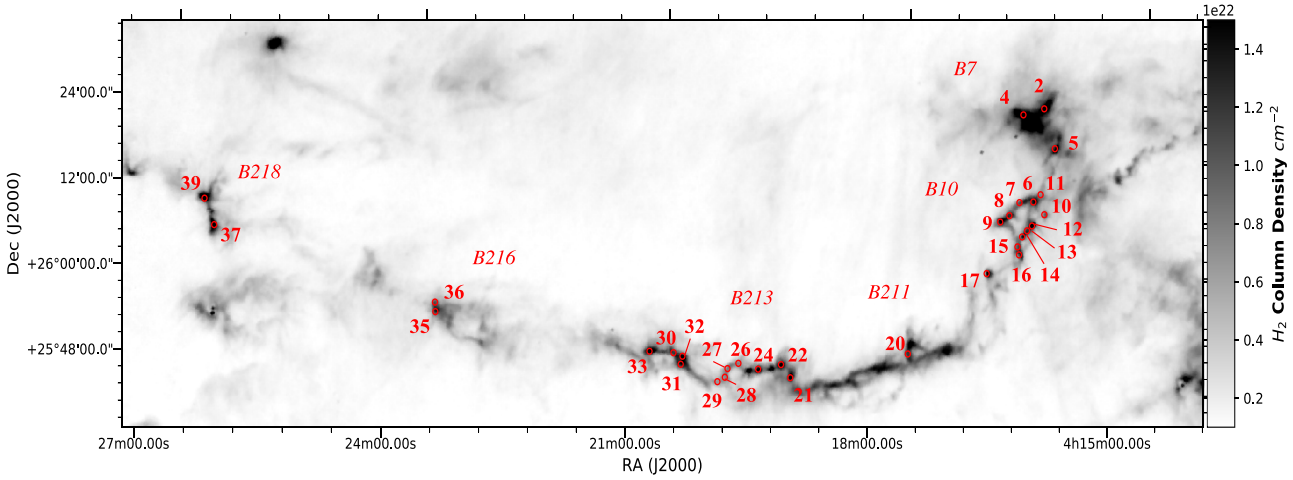

Figure 1. *Herschel*-derived H_2 column density map, presented in Marsh et al. (2016), of the B7, B10, B211, B213, B216, and B218 regions of the Taurus molecular cloud. The numbered circles in red represent the 31 cores targeted in this study. The circles have a diameter of 62.″3 (our CH_3OH beam size). Source selection was based on analysis of the ammonia NH_3 (1, 1) intensity map as described in Seo et al. (2015).

the idea that precursor molecules of COMs first form on the icy surfaces of interstellar grains and then get ejected into the gas via reactive desorption (Vasyunin & Herbst 2013; Balucani et al. 2015; Vasyunin et al. 2017). Unlike other processes, chemical desorption links the solid and gas phases without immediate interaction with any external agents, such as photons, electrons, or other energetic particles; in this process, the newly formed molecule possesses an energy surplus that allows it to evaporate (Minissale et al. 2016). This process can be efficient in the cold, UV-shielded environments of prestellar cores. Recent experimental laboratory studies found that reactive desorption can in fact occur in the conditions found in starless core environments (Chuang et al. 2018; Oba et al. 2018). Observations, like those presented in this paper, that place constraints on COM abundances are crucial to test chemical desorption models (i.e., Vasyunin et al. 2017).

Studies to date have all pointed to only a few (<10) well-known dense starless cores that may not necessarily be representative of average populations (i.e., L1544 is one of the densest, most evolved starless cores known). The lack of COM abundance measurements in a larger sample of cold cores has prevented testing of COM formation scenarios. In fact, only one prestellar core, L1544, has been thoroughly tested against chemical desorption models (Jiménez-Serra et al. 2016; Vasyunin et al. 2017). A study of a complete sample of starless cores within a molecular cloud is needed to constrain the question of how prevalent COMs are and what range of abundances are observed.

In this paper, we present observations of COMs in the gas phase toward the complete ammonia-identified sample of 31 starless and prestellar cores within the L1495-B218 filaments of the Taurus star-forming region (Figure 1). We first targeted methanol, CH_3OH, because it is one of the simplest and most abundant COMs (Tafalla et al. 2006). We then searched for the more complex molecule acetaldehyde (CH_3CHO). Our study is unique in that it has targeted a large sample of starless and prestellar cores, spanning a wide range of dynamical and chemical evolutionary stages, localized within a common region within a single cloud. A survey within one molecular cloud eliminates potential chemical differences found from comparing cores from different clouds. The cores in this survey all have similar environmental conditions that warrant a more robust comparison than heterogeneous surveys.

Table 1
Line Parameters

Molecule	Transition	Freq. (GHz)	E_{up} (K)	A_{ij} (s^{-1})
CH_3OH	$2_{-1,2}$–$1_{-1,1}$ E	96.739363	12.542	2.557E−6
	$2_{0,2}$–$1_{0,1}$ A^+	96.741377	6.965	3.408E−6
	$2_{0,2}$–$1_{0,1}$ E	96.744549	20.090	3.408E−6
CH_3CHO	$5_{0,5}$–$4_{0,4}$ E	95.947439	13.935	2.955E−5
	$5_{0,5}$–$4_{0,4}$ A	95.963465	13.838	2.954E−5
	$2_{1,2}$–$1_{0,1}$ A^{++}	84.219750	4.967	2.383E−6

Note. Taken from SLAIM (http://www.cv.nrao.edu/php/splat/).

In Section 2 we describe the Arizona Radio Observatory (ARO) data, along with our reduction techniques. We explain the source selection in Section 3. In Section 4 we discuss our observational results, calculate column densities and abundances for each molecular species, and analyze the chemical and evolutionary trends. In Section 5 we discuss the connection between the widespread precursor COM, methanol, and acetaldehyde.

2. Observations and Data Reduction

Molecular line observations for 31 cores within the L1495-B218 filament in the Taurus molecular cloud were taken with the ARO 12 m telescope on Kitt Peak. From previous ammonia survey results, we know that these cores have kinetic temperatures of 8–11 K, thermally dominated velocity dispersions of 0.08–0.24 km s^{-1}, and dust masses ranging from 0.05 to 9.5 $M_\odot$ (Tables 1 and 2 of Seo et al. 2015). Single-pointing observations were carried out from 2017 October to 2018 March in 50 shifts totaling around 411 hr. Three transitions of 2_k–1_k lines of methanol were targeted: CH_3OH E 2_{-1}–1_{-1} ($E_u/k = 12.5$ K) centered at 96.739 GHz, CH_3OH A^+ 2_0–1_0 ($E_u/k = 6.9$ K) centered at 96.741 GHz, and CH_3OH E 2_0–1_0 ($E_u/k = 20.1$ K) centered at 96.744 GHz. Additionally, three transitions of acetaldehyde ($5_{(0,5)}$–$4_{(0,4)}$ E and A, as well as the $2_{(1,2)}$–$1_{(0,1)}$ lines) were targeted (parameters listed in Table 1). Given an FWHM of 62.″3, the beam radius for our methanol

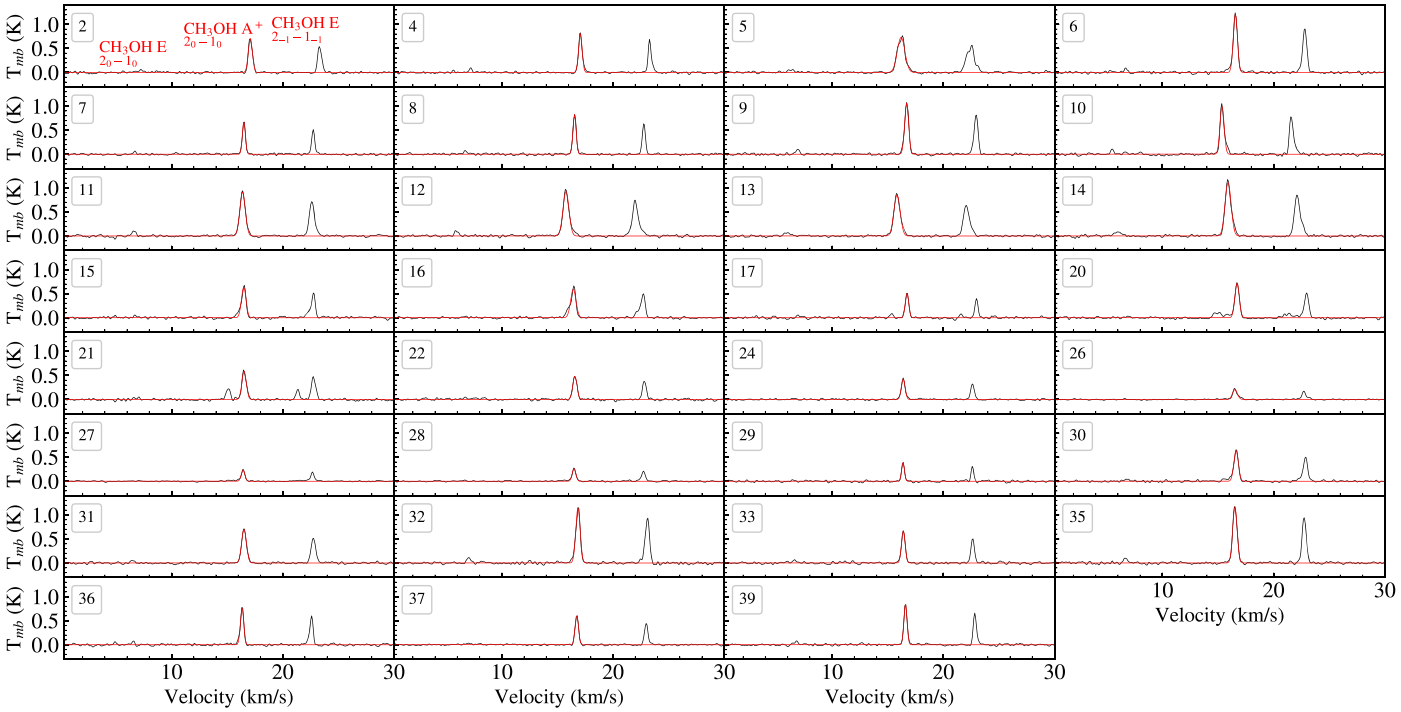

Figure 2. Spectra of methanol in the 31 prestellar cores in Taurus. Overplotted in red is the fit to the brightest CH_3OH A^+ line. Numbers in the top left panel correspond to the regions labeled in Figure 1. Note that the plotted velocity corresponds to the v_{LSR} of the weakest methanol line.

observations was 31.″15, or 0.02 pc, at a distance of 135 pc (Schlafly et al. 2014). Each scan was 5 minutes using absolute position switching (APS) between the source and the off position every 30 s. Observations of each source took ∼1, ∼3, and ∼6 hr for the 96 GHz lines of CH_3OH and CH_3CHO and the 84 GHz line of CH_3CHO, respectively. We pointed at the NH_3 peak position as tabulated in Seo et al. (2015). Pointing was checked every hour on a nearby quasar or planet. The system noise temperature was ∼150 K. The Millimeter Auto Correlator (MAC) instrument was used as the back end, with a bandwidth of 150 MHz and 24.4 kHz resolution with Hanning smoothing. The frequency resolution corresponds to a velocity resolution of ∼0.08 km s^{-1} at 96 GHz, which is narrower than the expected line width of these cores (∼0.3 km s^{-1}). These were dual polarization observations, providing two independent, simultaneous observations used to distinguish between false spectral features and real lines. Single-pointing spectra are plotted in Figures 2–4.

Data reduction was performed using the CLASS program of the GILDAS package.[1] Peak line fluxes, intensities, velocities, and line widths have been derived by Gaussian fits to the line profiles. Two separate beam efficiencies were determined from 34 planet (Jupiter, Mars, and Venus) observations taken over the course of our observation run. The median efficiency percentage for each planet was calculated, along with the estimated errors, for each polarization (called MAC11 and MAC12). The median beam efficiency value for the combination of the three planets was then applied to our observations in each separate channel. These channels were then summed together, giving us the main beam temperature scale, $T_{mb} = T_A^*/\eta$, where $\eta_{MAC11} = 0.861 \pm 0.006$ and $\eta_{MAC12} = 0.838 \pm 0.006$. Additionally, a factor of 1.14 needed to be multiplied to the final main beam temperature due to a systematic calibration error present in the software of the MAC, discovered after our APS observations were completed. The MAC antenna temperature was found to be 14% lower than the new, more trusted AROWS back end. This result only became available in 2018 April after APS observations were complete.

Before the new AROWS spectrometer was commissioned in 2018 April, on-the-fly (OTF) mapping was not possible with the MAC because data rates were too high (i.e., data could not be taken and stored simultaneously). We began the mapping of CH_3OH emission in 2018 May. Seven separate maps were observed toward the regions where most of the cores are located. We tuned to 96.741375 GHz in the lower sideband, choosing the 19.5 kHz mode on AROWS using only the central 1024 channels. We performed OTF mapping in 15′ × 15′ regions (see Figure 5), with each row spaced at 22″. The scan rate was 15″ s^{-1} with the OFF integration time at 36 s and calibration integration time at 5 s. We made multiple maps in the R.A. and decl. directions, later baselining and combining the maps within the CLASS software. For intensity mapping, the data were processed with a pipeline script in CLASS written by W. Peters (see Bieging & Peters 2011) that created 3D spectral cubes with a new convolved beam size of 81.″17. The program miriad[2] was then used to create integrated intensity (moment 0) maps (Figure 5). The resampling of OTF maps at lower resolution is needed so as to not miss information in the image field and to improve the signal-to-noise ratio. We present only single-pointing measurements for CH_3CHO because it was not bright enough to map; i.e., it would have taken ∼2000 hr to map the same 15′ × 15′ regions as we did for methanol or ∼5000 hr to map each core in the 2′ × 2′ regions to get down to 4 mK rms.

[1] http://iram.fr/IRAMFR/GILDAS/

[2] https://bima.astro.umd.edu/miriad/

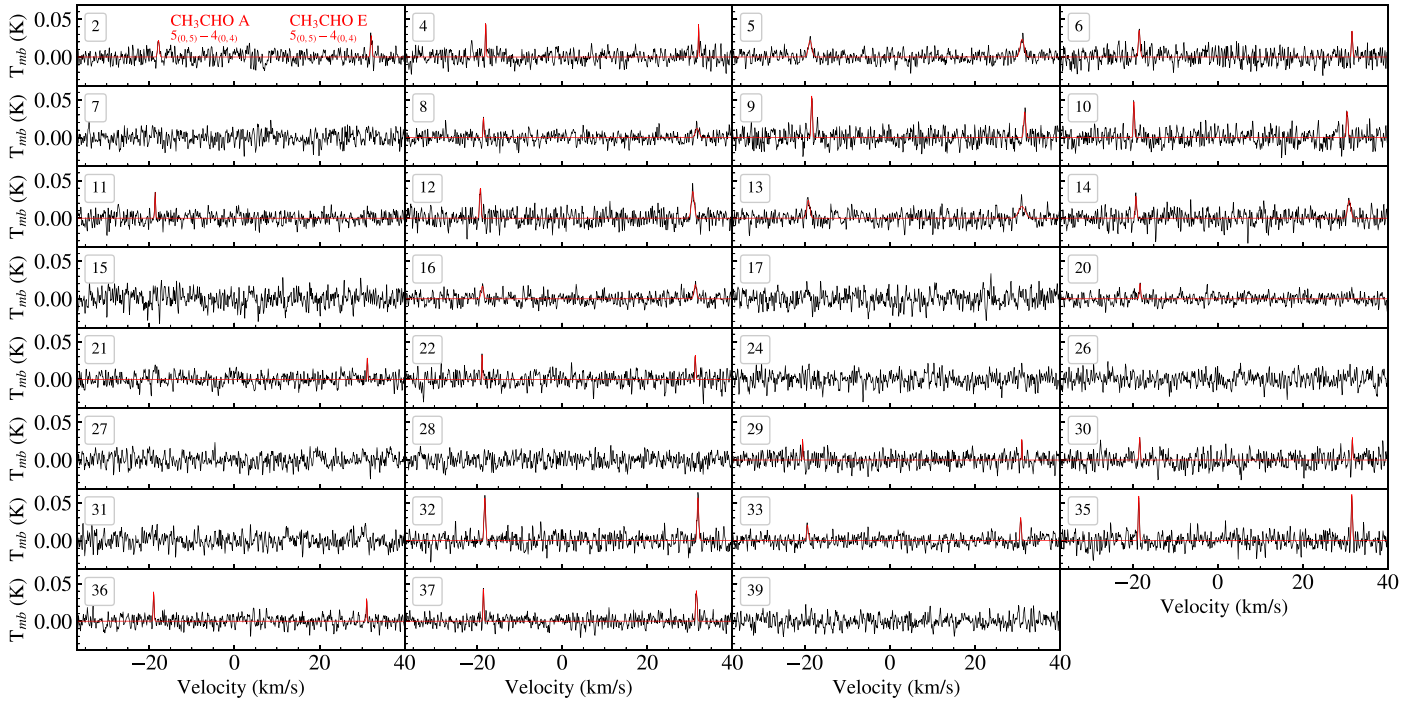

Figure 3. Spectra of the 96 GHz transitions of CH_3CHO in all 31 prestellar cores in Taurus (including nondetections). Numbers in the top left panel correspond to the regions labeled in Figure 1. Overplotted in red are fits to the detected lines. Spectra with no red fits are considered nondetections. Note that the plotted velocity is the v_{LSR} of the average of the A and E line frequencies.

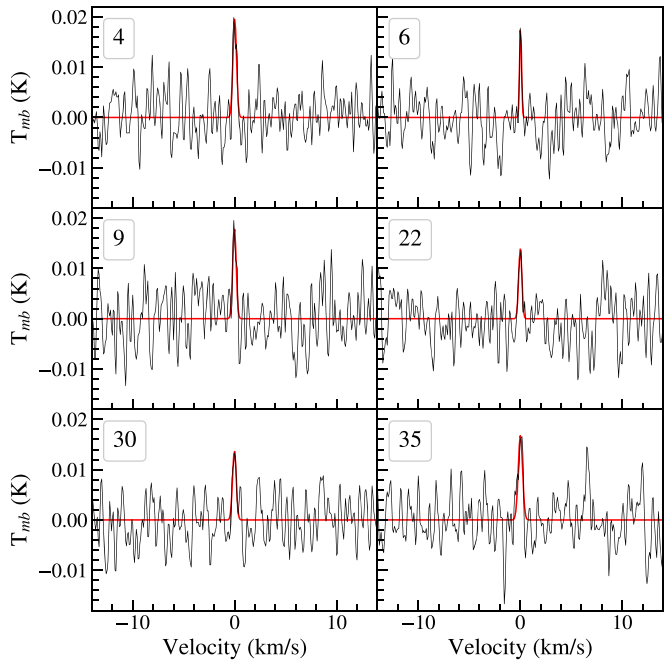

Figure 4. Spectra of the 84 GHz line of CH_3CHO and corresponding Gaussian fit in red for the six detected sources. The expected frequency of this transition was shifted to a v_{LSR} of 0 km s^{-1} for visual comparison. Numbers in the top left panel correspond to the cores labeled in Figure 1.

3. Source Selection

Sources were chosen from cores defined from the Cardiff Source-finding AlgoRithm (CSAR), as described in Kirk et al. (2013), performed on an ammonia NH_3 (1, 1) intensity map, as described by Seo et al. (2015). From the total 39 listed cores (leaves in the CSAR output), we discarded four sources that were observed to have protostars, three sources where the 12 m beams overlapped, and one source (L1495A-S) that had been previously studied in Bacmann & Faure (2016).

Calculations of column density and excitation temperature for the COMs detected require average volume density measurements for each core. Using our single-pointing beam size of 62.″3 (8410 au at 135 pc; Schlafly et al. 2014), we calculated the average volume density within each of the 31 cores using the line-of-sight distance of 135 pc and a median H_2 column density (N_{H_2}) from *Herschel* column density maps of Taurus, which have 18″ resolution (Palmeirim et al. 2013; Marsh et al. 2016). The median dust temperature from the corresponding *Herschel* temperature maps was also calculated. Within Ds9 (Joye & Mandel 2003), we overlaid the region files of our beam size onto the maps and recorded the median H_2 column density (N_{H_2}) and dust temperature (T_{dust}) values (Table 2). Due to limited resolution, we stress that by averaging core properties over the beam, we are making global measurements, since a detailed physical model of the sources from high-resolution (10″) dust data does not yet exist. Central core densities can be an order of magnitude denser than local volume density measurements; i.e., Seo12 is believed to have a central density of $\sim 10^6$ cm^{-3} (Tokuda et al. 2019), while its beam-averaged density reported in this paper is $\sim 10^5$ cm^{-3}. Thus, the high uncertainties of the physical source parameters (including kinematics, as well as density and temperature profiles) make direct comparisons between sources challenging if one attempted more advanced modeling techniques. The average ratio between our beam-averaged volume density and the volume density reported in Seo et al. (2015) is $\left\langle \frac{n_{\rm Beam}}{n_{\rm seo}} \right\rangle = 0.81$, with a standard deviation of 0.19 (the median is 0.76 with a median standard deviation of 0.14). Seo et al. (2015) assumed that the kinetic temperature was equal to the

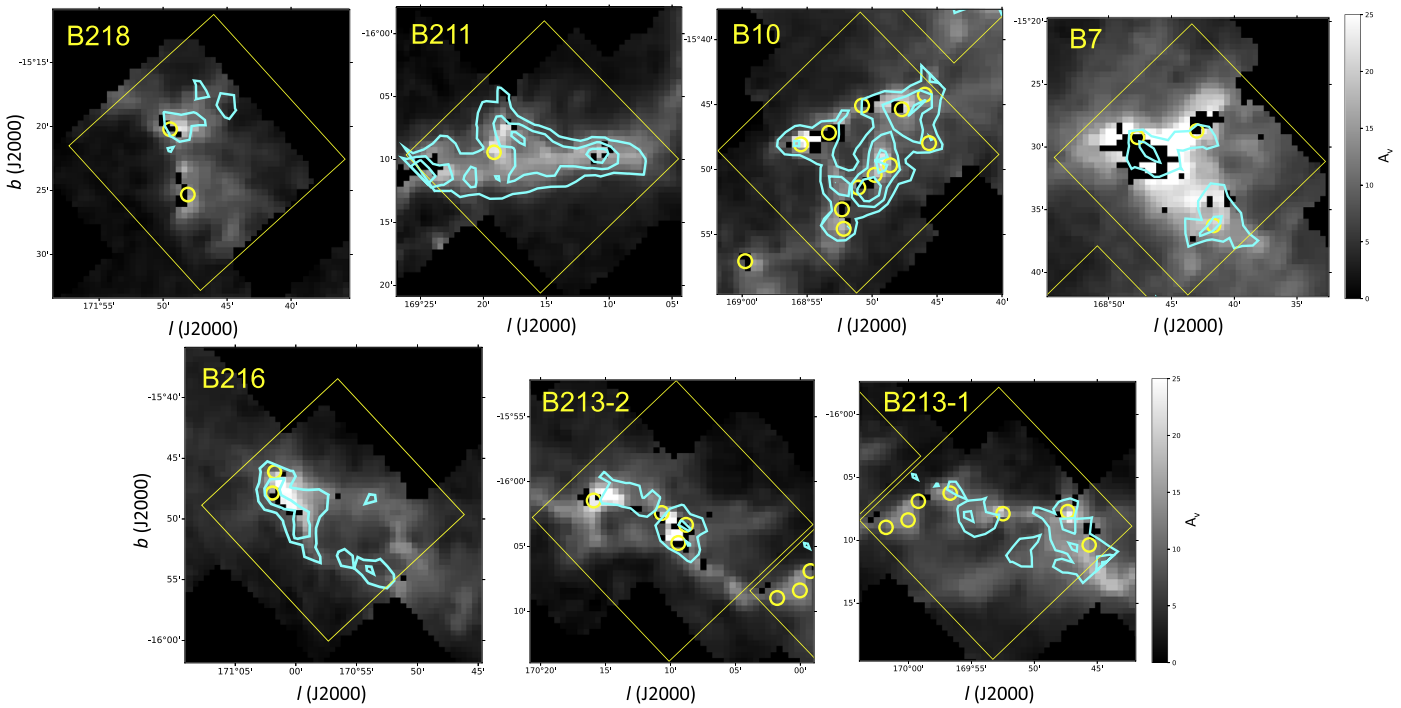

Figure 5. Methanol emission (cyan contours) overlaid on extinction maps (Schmalzl et al. 2010) of the B7/B10/B211/B213/B216/B218 regions of Taurus (axes in galactic coordinates l and b). The yellow boxes correspond to the $15' \times 15'$ size of our OTF maps, and the yellow circles represent the cores targeted in this study. The cyan contours within the boxes are plotted in steps of 0.2 K km s^{-1} ($\sim 2\sigma$ detection) created from the integrated intensity maps at a resolution of $81''$.

dust temperature, which is not true. Since spectral energy distribution fitting went into the calculation of the column density maps in the *Herschel* data, we use $n_{\rm Beam}$ in this paper. The NH_3 (1, 1) observations in Seo et al. (2015) only effectively probe density $>10^3$ cm^{-3} (Shirley 2015).

4. Results

We detected CH_3OH in 100% (31/31) of the cores targeted and CH_3CHO in 70% (22/31). In the following subsections, we discuss how we calculated molecular column densities for all cores and further discuss the distribution of methanol from our OTF mapping results. All values in Tables 2–8 are from the more sensitive single-pointing observations.

4.1. CH_3OH Column Densities

Methanol was detected in all 31 cores (Figure 2 and Table 3). The $v_{\rm LSR}$ of the methanol lines is consistent with that of the ammonia NH_3 (1, 1) line, and the ratio of NH_3 (1, 1) to the brightest CH_3OH A^+ 2_0–1_0 transition is, on average, 1.02. The median rms noise in the spectra is $\theta_{\rm mb} \sim 15$ mK. Due to its higher upper energy, CH_3OH E 2_0–1_0 is the weakest of the three lines and therefore not always detected. If this line was not detected above $>4\sigma$, we present upper limits (Table 3). As a test, we integrated on core Seo26 (one of the weak detection cores) four times as long ($\sim$4 hr versus $\sim$1 hr) to lower the rms to $\sim$6 mK to see if the weaker methanol line could be detected. Unfortunately, we were not able to confirm a detection, and an upper limit is still reported.

The brightest cores, determined from the brightest CH_3OH A^+ 2_0–1_0 transition, are (from brightest to weakest) Seo6, Seo32, Seo35, Seo14, and Seo9. The two brightest CH_3OH lines are clearly detected in all cores (to the 12σ–78σ level). The detection of more than one line of methanol shows the unambiguous presence of methanol in the cold gas within NH_3-detected starless cores.

Since we detected multiple lines of CH_3OH with different E_u/k values, we used the radiative transfer code RADEX to calculate column densities (see van der Tak et al. 2007). RADEX calculates an excitation temperature, $T_{\rm ex}$; a column density, N; and an opacity, τ, for each transition separately. A grid of RADEX models was created to find the best-fit column density. The difference in our observed line peak versus the line peak RADEX calculates was minimized in order to find the best fit. In the top panel of Figure 6, we show an example for core Seo15, where we plot the difference in radiation temperatures divided by the observed rms, written as $|T_{\rm mb} - T_{\rm radex}|/\sigma_T$, versus the column density N for each transition line. The best-fit column densities for all three methanol transitions fall within a factor of at most 1.3 of each other.

In RADEX calculations, there are three input parameters—volume density, $n_{\rm beam}$; gas kinetic temperature, $T_{\rm kin}$; and line width, FWHM—that were varied to get error estimates for column density. We input the average beam volume densities described in Section 3 into our RADEX calculations. The statistical volume density error was estimated to be 10% of our value, based on typical estimates of the statistical uncertainty in calculations of the column density of H_2 from *Herschel* maps (see Kirk et al. 2013). We point out that the dust opacity assumption could easily lead to a factor of 2–3 in the systematic uncertainty in volume density (Shirley et al. 2011). However, we find that even if our volume density calculations are off by an order of magnitude, we would only be a factor of $\sim$2 off in column density, as determined from RADEX calculations (Figure 6, bottom panel). The statistical error for $T_{\rm kin}$ came directly from Table 2 in Seo et al. (2015), and the statistical FWHM error came from our CLASS

Table 2
Physical Parameters

Core Number	α (J2000.0)	δ (J2000.0)	$n_{\rm beam}$ (cm^{-3})	$T_{\rm dust}$ (K)	$T_{\rm kin}$ (K)
2	4:18:33.1	+28:27:11.0	1.53E+05	11.28	$9.66^{+0.09}_{-0.08}$
4	4:18:45.9	+28:23:30.0	1.57E+05	13.06	$8.49^{+0.99}_{-0.99}$
5	4:18:04.2	+28:22:51.6	1.23E+05	12.10	$9.65^{+1.52}_{-1.34}$
6	4:17:52.8	+28:12:25.7	1.18E+05	11.46	$9.47^{+0.78}_{-0.5}$
7	4:18:02.6	+28:10:27.8	8.15E+04	11.76	$9.48^{+0.43}_{-0.55}$
8	4:18:03.7	+28:07:16.9	9.50E+04	11.42	$9.26^{+0.16}_{-0.21}$
9	4:18:07.0	+28:05:13.0	1.25E+05	11.10	$8.61^{+0.3}_{-0.24}$
10	4:17:37.6	+28:12:01.8	6.84E+04	12.39	$9.63^{+2.12}_{-2.11}$
11	4:17:51.2	+28:14:25.0	6.05E+04	12.42	$10^{+0.39}_{-0.54}$
12	4:17:41.7	+28:08:45.7	1.31E+05	11.17	$9.29^{+0.94}_{-0.38}$
13	4:17:42.2	+28:07:29.4	9.27E+04	11.62	$10.9^{+1.06}_{-1.41}$
14	4:17:42.9	+28:06:00.3	9.72E+04	11.65	$9.68^{+0.59}_{-0.37}$
15	4:17:41.0	+28:03:49.9	8.51E+04	11.97	$8.84^{+0.39}_{-0.5}$
16	4:17:36.1	+28:02:56.7	9.66E+04	11.81	$9.66^{+0.27}_{-0.3}$
17	4:17:50.3	+27:55:52.4	1.05E+05	11.34	$9.31^{+0.59}_{-0.54}$
20	4:18:07.8	+27:33:53.0	9.16E+04	11.59	$9.5^{+1.22}_{-1.29}$
21	4:19:23.3	+27:14:46.0	1.15E+05	11.86	$9.17^{+1.36}_{-1.3}$
22	4:19:37.1	+27:15:17.7	1.19E+05	11.35	$9.74^{+0.58}_{-0.75}$
24	4:19:51.4	+27:11:26.3	1.17E+05	10.88	$9.08^{+0.15}_{-0.16}$
26	4:20:09.6	+27:09:44.3	5.86E+04	11.95	$9.75^{+1.31}_{-1.22}$
27	4:20:14.7	+27:07:38.8	6.00E+04	11.93	$10.3^{+1.01}_{-1.09}$
28	4:20:12.2	+27:06:02.3	5.73E+04	11.86	$11.3^{+0.99}_{-1.31}$
29	4:20:15.4	+27:04:23.2	5.01E+04	11.95	$10^{+0.67}_{-0.97}$
30	4:21:02.5	+27:02:30.4	9.08E+04	11.42	$9.92^{+1.08}_{-1.18}$
31	4:20:51.6	+27:01:53.6	1.04E+05	11.34	$9.55^{+0.49}_{-0.52}$
32	4:20:54.0	+27:03:13.0	1.28E+05	11.09	$8.95^{+1.96}_{-1.32}$
33	4:21:21.6	+26:59:30.6	1.35E+05	10.60	$9.54^{+0.93}_{-0.58}$
35	4:24:20.5	+26:36:02.1	8.97E+04	11.34	$9.22^{+0.8}_{-1.11}$
36	4:24:25.2	+26:37:15.7	7.24E+04	11.69	$9.81^{+1.62}_{-0.92}$
37	4:27:47.4	+26:17:57.8	1.29E+05	10.85	$9.83^{+0.5}_{-0.62}$
39	4:28:09.2	+26:20:27.7	1.71E+05	10.56	$9.55^{+0.68}_{-0.56}$

Note. Physical parameters from *Herschel* column density and temperature maps, i.e., average volume density ($n_{\rm beam}$) and average dust temperature ($T_{\rm dust}$), as well as the gas kinetic temperature from ammonia maps taken from Table 2 of Seo et al. (2015; $T_{\rm kin}$).

Gaussian fits (Table 3). In a test case, we plotted all 27 statistical error combinations (each parameter having a plus and minus error) and found that the combination of all "plus" values and the combination of all "minus" values gave the widest difference in column density in the grids. Therefore, we adopted this error combination when calculating our statistical errors for the remaining cores.

In general, all lines have been minimized around a similar column density (within a factor of ∼1.3). However, in some cases, we did not detect the third line, or the third line was only an upper limit, so our column density becomes uncertain (large errors). In Table 6 we present this minimized, or "best-fit," column density for all three transitions separately, as well as a total column density, $N_{\rm tot}$, which is a sum of the two brightest transitions (excluding the weakest E state).

As a consistency check, we compared our RADEX-determined column densities to the commonly used method for calculating column density from an optically thin line. The CTEX method (constant $T_{\rm ex}$) assumes a constant excitation temperature when converting from the column density in the upper level of the transition to all energy levels (see details in the Appendix of Caselli et al. 2002 and Equation (80) of Mangum & Shirley 2015). We calculated CTEX column densities for the brightest CH_3OH A^+ 2_0–1_0 transition assuming the $T_{\rm ex}$ determined from RADEX calculations. We found that the RADEX-determined column densities all agree with the CTEX-determined column densities, and the median ratio is 1.08 with a median standard deviation of 0.03.

The total column density, $N_{\rm tot}$, from Table 6 is in the range (0.42–3.4) × 10^{13} cm^{-2}. Excitation temperatures range from $T_{\rm ex}$ = 6.8 to 8.7 K, and optical depths are consistent with optically thin $\tau < 0.3$ (see Table 6). We found that, on average, the A:E column density ratio is 1.3, with a median absolute standard deviation of 0.03. This ratio agrees with the Harju et al. (2019) A:E ratio of 1.2–1.5 observed for the starless core H-MM1 in Ophiuchus.

4.1.1. CH_3OH Abundance Trends

We found total CH_3OH abundances (A+E species with respect to H_2) for the 31 cores in the range (0.525–3.36) × 10^{-9}. Our observed abundances are comparable to published values toward other prestellar cores (Tafalla et al. 2006; Vastel et al. 2014; Soma et al. 2015; Punanova et al. 2018). The Seo et al. (2015) paper analyzed which regions in L1495-B218 were more or less evolved by searching for the presence of protostars (class 0, I, or II) within the regions.

Table 3
Methanol Gaussian Fit Results

Core	CH_3OH E 2_0–1_0 Area (K km s^{-1})	Vel. (km s^{-1})	FWHM (km s^{-1})	T_{mb} (K)	CH_3OH A 2_0–1_0 Area (K km s^{-1})	Vel. (km s^{-1})	FWHM (km s^{-1})	T_{mb} (K)	CH_3OH E 2_{-1}–1_{-1} Area (K km s^{-1})	Vel. (km s^{-1})	FWHM (km s^{-1})	T_{mb} (K)	rms (K)
2.0	[a]0.026(0.005)	7.211(0.063)	0.607(0.184)	0.0402	0.322(0.012)	7.248(0.008)	0.426(0.019)	0.71	0.245(0.003)	7.2355(0.003)	0.425(0.006)	0.542	0.0146
4.0	0.0292(0.003)	7.191(0.013)	0.277(0.032)	0.0992	0.325(0.013)	7.224(0.007)	0.377(0.018)	0.81	0.238(0.003)	7.2165(0.002)	0.341(0.006)	0.656	0.0138
5.0	0.0408(0.005)	6.308(0.037)	0.703(0.1)	0.0545	0.624(0.023)	6.367(0.015)	0.802(0.034)	0.731	0.484(0.005)	6.3565(0.004)	0.877(0.011)	0.518	0.013
6.0	0.0306(0.004)	6.709(0.018)	0.318(0.046)	0.0905	0.566(0.021)	6.723(0.008)	0.436(0.02)	1.22	0.424(0.004)	6.7155(0.002)	0.44(0.005)	0.905	0.0153
7.0	0.018(0.003)	6.693(0.018)	0.253(0.043)	0.0666	0.231(0.009)	6.67(0.006)	0.318(0.015)	0.684	0.175(0.003)	6.6565(0.003)	0.324(0.007)	0.507	0.0129
8.0	0.0272(0.005)	6.725(0.026)	0.361(0.101)	0.0708	0.299(0.011)	6.705(0.006)	0.34(0.015)	0.826	0.224(0.003)	6.6905(0.002)	0.327(0.005)	0.643	0.013
9.0	0.0426(0.004)	6.903(0.016)	0.385(0.036)	0.104	0.483(0.018)	6.866(0.008)	0.427(0.019)	1.06	0.366(0.003)	6.8605(0.002)	0.421(0.004)	0.818	0.0136
10.0	0.0362(0.004)	5.481(0.017)	0.301(0.039)	0.113	0.466(0.019)	5.525(0.008)	0.435(0.022)	1.01	0.352(0.005)	5.5195(0.003)	0.43(0.007)	0.769	0.016
11.0	0.0472(0.004)	6.617(0.018)	0.417(0.042)	0.106	0.563(0.022)	6.549(0.011)	0.578(0.026)	0.915	0.416(0.004)	6.5385(0.003)	0.552(0.007)	0.707	0.0139
12.0	0.048(0.004)	5.919(0.017)	0.416(0.035)	0.108	0.621(0.025)	5.933(0.012)	0.627(0.03)	0.93	0.475(0.005)	5.9225(0.003)	0.639(0.009)	0.698	0.0152
13.0	0.049(0.005)	5.967(0.032)	0.684(0.072)	0.0673	0.6(0.022)	6(0.012)	0.659(0.03)	0.855	0.436(0.004)	5.9955(0.003)	0.662(0.008)	0.619	0.013
14.0	0.073(0.006)	5.998(0.033)	0.827(0.08)	0.0829	0.755(0.028)	6.067(0.012)	0.637(0.029)	1.11	0.558(0.005)	6.0535(0.003)	0.645(0.007)	0.814	0.0147
15.0	[a]0.0162(0.004)	6.724(0.031)	0.275(0.097)	0.0553	0.328(0.013)	6.656(0.01)	0.484(0.025)	0.637	0.233(0.005)	6.6545(0.005)	0.451(0.013)	0.485	0.0149
16.0	…	…	…	…	0.36(0.015)	6.592(0.012)	0.568(0.032)	0.595	0.267(0.004)	6.5885(0.004)	0.545(0.01)	0.46	0.0116
17.0	[a]0.0279(0.005)	7.025(0.058)	0.569(0.111)	0.0461	0.2(0.008)	6.898(0.007)	0.365(0.018)	0.514	0.137(0.004)	6.8985(0.005)	0.326(0.012)	0.396	0.017
20.0	…	…	…	…	0.357(0.014)	6.876(0.009)	0.466(0.021)	0.72	0.253(0.006)	6.8785(0.005)	0.469(0.013)	0.507	0.0219
21.0	[a]0.0245(0.004)	6.844(0.063)	0.649(0.112)	0.0354	0.293(0.014)	6.685(0.011)	0.466(0.027)	0.59	0.229(0.008)	6.6845(0.008)	0.465(0.019)	0.463	0.0291
22.0	…	…	…	…	0.23(0.009)	6.732(0.009)	0.442(0.02)	0.488	0.167(0.004)	6.7365(0.005)	0.405(0.011)	0.388	0.0143
24.0	…	…	…	…	0.181(0.007)	6.554(0.007)	0.395(0.02)	0.43	0.13(0.002)	6.5375(0.003)	0.378(0.008)	0.324	0.0101
26.0	[a]0.00588(0.001)	6.606(0.023)	0.213(0.059)	0.0259	0.114(0.005)	6.688(0.011)	0.514(0.031)	0.208	0.0794(0.002)	6.6445(0.006)	0.466(0.02)	0.16	0.00706
27.0	…	…	…	…	0.0957(0.004)	6.591(0.008)	0.377(0.021)	0.239	0.0753(0.002)	6.5875(0.005)	0.393(0.015)	0.18	0.00737
28.0	[a]0.00807(0.002)	6.653(0.036)	0.299(0.09)	0.0253	0.109(0.005)	6.655(0.008)	0.386(0.022)	0.264	0.0887(0.003)	6.6465(0.006)	0.417(0.015)	0.2	0.00882
29.0	…	…	…	…	0.125(0.006)	6.54(0.006)	0.297(0.015)	0.396	0.0895(0.003)	6.5315(0.005)	0.267(0.01)	0.314	0.0141
30.0	[a]0.0262(0.004)	6.786(0.041)	0.583(0.108)	0.0422	0.324(0.013)	6.791(0.009)	0.475(0.023)	0.64	0.246(0.004)	6.7775(0.003)	0.473(0.009)	0.488	0.0124
31.0	0.0238(0.003)	6.491(0.029)	0.4(0.055)	0.056	0.376(0.014)	6.679(0.009)	0.499(0.022)	0.707	0.27(0.004)	6.6695(0.003)	0.489(0.008)	0.519	0.0134
32.0	0.0501(0.004)	7.029(0.016)	0.417(0.034)	0.113	0.565(0.023)	7.012(0.009)	0.463(0.022)	1.15	0.453(0.005)	6.9995(0.002)	0.461(0.006)	0.924	0.0169
33.0	[a]0.027(0.005)	6.618(0.031)	0.411(0.098)	0.0617	0.273(0.011)	6.567(0.007)	0.385(0.018)	0.667	0.198(0.004)	6.5575(0.003)	0.366(0.008)	0.509	0.0157
35.0	0.0454(0.005)	6.679(0.021)	0.403(0.046)	0.106	0.583(0.023)	6.682(0.009)	0.464(0.021)	1.18	0.446(0.004)	6.6675(0.002)	0.439(0.005)	0.954	0.0166
36.0	0.0225(0.004)	6.552(0.022)	0.25(0.043)	0.0844	0.293(0.012)	6.508(0.007)	0.353(0.017)	0.78	0.22(0.004)	6.4955(0.003)	0.356(0.008)	0.581	0.0156
37.0	[a]0.0147(0.003)	6.973(0.045)	0.522(0.106)	0.0265	0.234(0.009)	6.904(0.006)	0.357(0.015)	0.616	0.174(0.003)	6.9005(0.003)	0.367(0.006)	0.445	0.00992
39.0	0.0343(0.004)	6.764(0.026)	0.473(0.069)	0.0682	0.305(0.012)	6.759(0.006)	0.339(0.016)	0.846	0.233(0.003)	6.7545(0.002)	0.337(0.005)	0.648	0.0135

Notes. Gaussian fits for the three methanol lines observed. Errors are reported in parentheses next to the number.
[a] Upper limits ($<4\sigma_{rms}$).

Table 4
Acetaldehyde $5_{(0,5)}$–$4_{(0,4)}$ Gaussian Fit Results

Core	CH_3CHO A $5_{(0,5)}$–$4_{(0,4)}$ Area (K km s^{-1})	Vel. (km s^{-1})	FWHM (km s^{-1})	T_{mb} (K)	CH_3CHO E $5_{(0,5)}$–$4_{(0,4)}$ Area (K km s^{-1})	Vel. (km s^{-1})	FWHM (km s^{-1})	T_{mb} (K)	rms (K)
2	0.0112(0.002)	7.379(0.043)	0.477(0.087)	0.022	0.0125(0.002)	7.241(0.031)	0.415(0.051)	0.0284	0.00662
4	0.0119(0.001)	7.257(0.015)	0.239(0.033)	0.0469	0.00963(0.001)	7.172(0.014)	0.208(0.036)	0.0435	0.00713
5	0.0232(0.003)	6.451(0.05)	0.998(0.15)	0.0218	0.0274(0.003)	6.174(0.053)	1.08(0.145)	0.0238	0.00573
6	0.0187(0.003)	6.782(0.033)	0.496(0.104)	0.0354	0.0123(0.002)	6.669(0.024)	0.326(0.048)	0.0355	0.00816
7	…	…	…	…	…	…	…	…	0.00744
8	0.00747(0.001)	6.732(0.022)	0.256(0.054)	0.0274	[a]0.0139(0.002)	6.844(0.097)	1.04(0.186)	[a]0.0126	0.00595
9	0.0227(0.002)	6.858(0.019)	0.386(0.039)	0.0554	0.0179(0.003)	6.774(0.042)	0.494(0.109)	0.0341	0.00826
10	0.0179(0.002)	5.526(0.022)	0.352(0.045)	0.0479	0.0169(0.002)	5.513(0.032)	0.454(0.065)	0.0351	0.0083
11	0.00929(0.001)	6.598(0.018)	0.251(0.042)	0.0348	…	…	…	…	0.0066
12	0.0174(0.002)	5.982(0.025)	0.41(0.05)	0.0399	0.0302(0.003)	5.808(0.04)	0.799(0.088)	0.0355	0.00789
13	[a]0.022(0.003)	6.035(0.051)	0.871(0.121)	0.0237	[a]0.0299(0.005)	6.122(0.132)	1.8(0.398)	0.0156	0.00716
14	[a]0.0121(0.002)	6.016(0.034)	0.386(0.097)	0.0293	[a]0.0223(0.003)	6.009(0.055)	0.894(0.126)	0.0234	0.00795
15	…	…	…	…	…	…	…	…	0.00937
16	[a]0.0118(0.002)	6.463(0.067)	0.668(0.128)	0.0166	[a]0.0138(0.002)	6.392(0.06)	0.685(0.156)	0.0189	0.00608
17	…	…	…	…	…	…	…	…	0.00608
20	[a]0.00814(0.001)	6.966(0.034)	0.375(0.089)	0.0204	…	…	…	…	0.00558
21	…	…	…	…	0.00728(0.001)	6.347(0.022)	0.235(0.044)	0.0291	0.00671
22	0.00779(0.002)	6.41(0.023)	0.217(0.056)	0.0337	0.00957(0.002)	6.381(0.025)	0.277(0.059)	0.0324	0.00773
24	…	…	…	…	…	…	…	…	0.00769
26	…	…	…	…	…	…	…	…	0.00769
27	…	…	…	…	…	…	…	…	0.00727
28	…	…	…	…	…	…	…	…	0.00702
29	0.00592(0.001)	4.71(0.023)	0.202(0.06)	0.0275	0.00502(0.001)	6.115(0.019)	0.165(0.04)	0.0285	0.00728
30	0.00966(0.002)	6.892(0.029)	0.3(0.062)	0.0303	0.00704(0.002)	6.763(0.025)	0.218(0.049)	0.0304	0.00821
31	…	…	…	…	…	…	…	…	0.00776
32	0.0273(0.002)	7.053(0.017)	0.452(0.041)	0.0567	0.0276(0.003)	7.007(0.02)	0.457(0.054)	0.0567	0.0077
33	0.0105(0.002)	5.833(0.046)	0.477(0.136)	0.0206	0.0114(0.001)	5.829(0.022)	0.342(0.04)	0.0314	0.00594
35	0.02(0.002)	6.684(0.014)	0.318(0.029)	0.059	0.0219(0.002)	6.63(0.016)	0.336(0.033)	0.0613	0.00787
36	0.0114(0.001)	6.245(0.016)	0.276(0.036)	0.0389	0.00697(0.001)	6.19(0.019)	0.216(0.046)	0.0304	0.00622
37	0.0128(0.001)	6.721(0.015)	0.272(0.033)	0.0442	0.0185(0.002)	6.637(0.02)	0.429(0.038)	0.0405	0.00609
39	…	…	…	…	…	…	…	…	0.0069

Notes. Gaussian fits for the two acetaldehyde lines observed in the 95.9 GHz range. Errors are reported in parentheses next to the number.
[a] Upper limits ($\lesssim 4\sigma_{rms}$). A total of 18 of the 31 cores had one or more of the $5_{(0,5)}$–$4_{(0,4)}$ lines detected with significance.

Table 5
Acetaldehyde (2_0–1_0) Gaussian Fit Results

Core	Area (K km s^{-1})	Vel. (km s^{-1})	FWHM (km s^{-1})	T_{mb} (K)	rms (K)
4	8.68E−03 (0.001)	7.143 (0.029)	0.418 (0.054)	1.950E−02	4.28E−03
6	4.46E−03 (0.001)	6.647 (0.024)	0.230 (0.056)	1.82E−02	4.13E−03
9	8.03E−03 (0.001)	6.766 (0.037)	0.414 (0.080)	1.82E−02	5.13E−03
22	6.27E−03 (0.001)	6.54 (0.038)	0.403 (0.085)	1.46E−02	4.254E−03
30	6.73E−03 (0.001)	6.595 (0.043)	0.447(0.102)	1.42E−02	4.270E−03
35	8.74E−03 (0.001)	6.550 (0.046)	0.493 (0.093)	1.67E−02	4.277E−03

Note. See Figure 4.

They found that regions B7, B213, and B218 are more evolved, and regions B10, B211, and B216 are less evolved (containing only starless and prestellar cores). In the left panel of Figure 7, we find that the less evolved regions typically have a higher methanol abundance, i.e., a median methanol abundance (with regard to H_2) of 1.48×10^{-9}, versus the more evolved regions, which have a median abundance 0.72×10^{-9}. This result is consistent with the picture that the methanol has "peaked" away (i.e., has a maximum abundance offset) from the center of the core in more evolved regions (as seen in L1544; Bizzocchi et al. 2014; Punanova et al. 2018), and we have probed the regions where methanol is depleted within a significant fraction of our beam.

We plot calculated abundances versus the virial parameter α, which tells us if our cores are gravitationally bound (ignoring external pressure, magnetic fields, and mass flow across the core boundary terms). The virial parameter is defined as

$$\alpha = \left| \frac{2\Omega_K}{\Omega_G} \right| = \frac{5\sigma^2 R_{\rm eff}}{GM}, \quad (1)$$

Table 6
Methanol Column Densities (cm^{-2}), Excitation Temperatures (K), and Optical Depths τ

Core	CH_3OH A 2_0–1_0 N (10^{13} cm^{-2})	T_{ex} (K)	τ	CH_3OH E 2_{-1}–1_{-1} N (10^{13} cm^{-2})	T_{ex} (K)	τ	CH_3OH E 2_0–1_0 N (10^{13} cm^{-2})	T_{ex} (K)	τ	Sum_{A+E}(Std) N_{tot} (10^{13} cm^{-2})
2	$0.735^{+0.03}_{-0.03}$	$8.33^{+0.415}_{-0.41}$	$0.1358^{+0.0055}_{-0.0055}$	$0.7^{+0.015}_{-0.01}$	$8.328^{+0.001}_{-<0.001}$	$0.1101^{+0.0023}_{-0.0016}$	[a]$0.71^{+0.18}_{-0.19}$	$8.329^{+2.02}_{-2.03}$	$0.01251^{+0.00321}_{-0.00337}$	1.4(0.035)
4	$0.79^{+<0.001}_{-0.025}$	$7.393^{+0.324}_{-0.327}$	$0.1941^{+<0.001}_{-0.0061}$	$0.715^{+0.005}_{-0.03}$	$7.388^{+0.001}_{-0.002}$	$0.1666^{+0.0011}_{-0.0069}$	$0.85^{+<0.001}_{-0.01}$	$7.397^{+1.57}_{-1.57}$	$0.03653^{+<0.001}_{-<0.001}$	1.5(0.075)
5	$1.425^{+0.01}_{-0.045}$	$8.079^{+0.47}_{-0.472}$	$0.1452^{+0.0011}_{-0.0046}$	$1.37^{+0.005}_{-0.05}$	$8.077^{+<0.001}_{-0.002}$	$0.1108^{+<0.001}_{-0.004}$	$1.22^{+0.035}_{-0.02}$	$8.072^{+2.1}_{-2.1}$	$0.01895^{+<0.001}_{-<0.001}$	2.8(0.055)
6	$1.375^{+0.015}_{-0.02}$	$7.926^{+0.482}_{-0.478}$	$0.2637^{+0.0028}_{-0.0037}$	$1.265^{+0.01}_{-0.01}$	$7.918^{+<0.001}_{-0.001}$	$0.2098^{+0.0017}_{-0.0016}$	$0.935^{+0.05}_{-0.07}$	$7.896^{+2.04}_{-2.05}$	$0.03293^{+0.0018}_{-0.00251}$	2.6(0.11)
7	$0.535^{+0.015}_{-0.005}$	$7.369^{+0.548}_{-0.544}$	$0.1539^{+0.0042}_{-0.0014}$	$0.5^{+<0.001}_{-0.005}$	$7.364^{+<0.001}_{-<0.001}$	$0.1273^{+<0.001}_{-0.0013}$	$0.64^{+0.06}_{-0.065}$	$7.384^{+2.06}_{-2.07}$	$0.02944^{+0.00279}_{-0.00303}$	1.0(0.035)
8	$0.705^{+0.025}_{-0.02}$	$7.457^{+0.495}_{-0.488}$	$0.1878^{+0.0065}_{-0.0053}$	$0.65^{+0.005}_{-<0.001}$	$7.45^{+0.001}_{-<0.001}$	$0.1602^{+0.0012}_{-<0.001}$	$0.925^{+0.2}_{-0.22}$	$7.483^{+2.02}_{-2.03}$	$0.02969^{+0.00653}_{-0.00714}$	1.4(0.055)
9	$1.21^{+0.025}_{-0.03}$	$7.304^{+0.39}_{-0.385}$	$0.2653^{+0.0054}_{-0.0064}$	$1.12^{+0.005}_{-0.005}$	$7.298^{+<0.001}_{-0.001}$	$0.2176^{+0.001}_{-0.001}$	$1.34^{+0.04}_{-0.045}$	$7.313^{+1.72}_{-1.72}$	$0.04156^{+0.00127}_{-0.00143}$	2.3(0.09)
10	$1.125^{+0.04}_{-0.185}$	$7.231^{+0.598}_{-0.632}$	$0.2406^{+0.0083}_{-0.0383}$	$1.045^{+0.055}_{-0.18}$	$7.221^{+0.007}_{-0.022}$	$0.207^{+0.0106}_{-0.0345}$	$1.365^{+0.01}_{-0.11}$	$7.26^{+2.1}_{-2.1}$	$0.05407^{+<0.001}_{-0.00444}$	2.2(0.08)
11	$1.335^{+0.025}_{-<0.001}$	$7.234^{+0.662}_{-0.658}$	$0.2136^{+0.0039}_{-<0.001}$	$1.22^{+0.015}_{-0.035}$	$7.222^{+0.002}_{-0.004}$	$0.189^{+0.0023}_{-0.0053}$	$1.835^{+0.07}_{-0.05}$	$7.287^{+2.19}_{-2.19}$	$0.0523^{+0.00203}_{-0.00144}$	2.6(0.12)
12	$1.47^{+0.02}_{-0.04}$	$7.873^{+0.433}_{-0.429}$	$0.1986^{+0.0026}_{-0.0053}$	$1.39^{+0.005}_{-<0.001}$	$7.87^{+<0.001}_{-<0.001}$	$0.1594^{+<0.001}_{-<0.001}$	$1.415^{+0.015}_{-0.025}$	$7.871^{+1.94}_{-1.94}$	$0.03844^{+<0.001}_{-<0.001}$	2.9(0.08)
13	$1.335^{+0.03}_{-0.015}$	$8.664^{+0.649}_{-0.648}$	$0.1498^{+0.0033}_{-0.0016}$	$1.21^{+<0.001}_{-0.035}$	$8.657^{+<0.001}_{-0.002}$	$0.1194^{+<0.001}_{-0.0034}$	$1.55^{+0.045}_{-<0.001}$	$8.676^{+2.71}_{-2.72}$	$0.02349^{+<0.001}_{-<0.001}$	2.5(0.12)
14	$1.8^{+0.035}_{-0.035}$	$7.827^{+0.545}_{-0.539}$	$0.2393^{+0.0045}_{-0.0046}$	$1.635^{+0.01}_{-0.015}$	$7.818^{+0.001}_{-0.001}$	$0.1905^{+0.0012}_{-0.0017}$	$2.385^{+0.06}_{-0.08}$	$7.859^{+2.22}_{-2.22}$	$0.03243^{+<0.001}_{-0.00111}$	3.4(0.17)
15	$0.78^{+0.02}_{-0.005}$	$6.982^{+0.465}_{-0.462}$	$0.1589^{+0.004}_{-0.001}$	$0.68^{+0.005}_{-0.005}$	$6.972^{+0.001}_{-0.001}$	$0.134^{+<0.001}_{-<0.001}$	[a]$0.595^{+0.155}_{-0.18}$	$6.963^{+1.79}_{-1.81}$	$0.02612^{+0.0069}_{-0.00796}$	1.5(0.1)
16	$0.815^{+0.035}_{-0.035}$	$7.754^{+0.521}_{-0.515}$	$0.1234^{+0.0053}_{-0.0052}$	$0.75^{+0.01}_{-0.005}$	$7.749^{+0.001}_{-<0.001}$	$0.105^{+0.0014}_{-<0.001}$	⋯	⋯	⋯	1.6(0.065)
17	$0.455^{+0.01}_{-0.01}$	$7.599^{+0.462}_{-0.459}$	$0.1106^{+0.0024}_{-0.0024}$	$0.385^{+0.01}_{-0.005}$	$7.591^{+0.001}_{-<0.001}$	$0.09242^{+0.00237}_{-0.00119}$	[a]$0.91^{+0.1}_{-0.115}$	$7.648^{+2.05}_{-2.05}$	$0.01816^{+0.00202}_{-0.00232}$	0.84(0.07)
20	$0.825^{+<0.001}_{-0.035}$	$7.567^{+0.522}_{-0.526}$	$0.157^{+<0.001}_{-0.0065}$	$0.72^{+0.005}_{-0.03}$	$7.558^{+0.001}_{-0.002}$	$0.1216^{+<0.001}_{-0.005}$	⋯	⋯	⋯	1.5(0.1)
21	$0.675^{+0.005}_{-0.015}$	$7.612^{+0.435}_{-0.436}$	$0.1284^{+<0.001}_{-0.0028}$	$0.655^{+0.005}_{-0.015}$	$7.61^{+0.001}_{-0.001}$	$0.1093^{+<0.001}_{-0.0024}$	[a]$0.775^{+0.04}_{-0.03}$	$7.619^{+1.94}_{-1.95}$	$0.01353^{+<0.001}_{-<0.001}$	1.3(0.02)
22	$0.51^{+0.015}_{-0.005}$	$8.093^{+0.471}_{-0.469}$	$0.09429^{+0.00274}_{-<0.001}$	$0.465^{+0.01}_{-<0.001}$	$8.09^{+<0.001}_{-<0.001}$	$0.08152^{+0.00173}_{-<0.001}$	⋯	⋯	⋯	0.97(0.045)
24	$0.41^{+0.02}_{-0.015}$	$7.549^{+0.419}_{-0.415}$	$0.09316^{+0.00451}_{-0.00338}$	$0.365^{+0.005}_{-0.005}$	$7.545^{+0.001}_{-<0.001}$	$0.07583^{+0.00103}_{-0.00104}$	⋯	⋯	⋯	0.78(0.045)
26	$0.255^{+<0.001}_{-0.005}$	$6.9^{+0.608}_{-0.609}$	$0.0488^{+<0.001}_{-<0.001}$	$0.22^{+<0.001}_{-0.005}$	$6.895^{+<0.001}_{-0.001}$	$0.04309^{+<0.001}_{-<0.001}$	[a]$0.235^{+0.04}_{-0.04}$	$6.898^{+1.95}_{-1.95}$	$0.01326^{+0.00226}_{-0.00227}$	0.47(0.035)
27	$0.21^{+0.005}_{-<0.001}$	$7.269^{+0.67}_{-0.669}$	$0.05116^{+0.00121}_{-<0.001}$	$0.205^{+<0.001}_{-0.005}$	$7.268^{+<0.001}_{-0.001}$	$0.04433^{+<0.001}_{-0.00107}$	⋯	⋯	⋯	0.41(0.005)
28	$0.23^{+0.005}_{-<0.001}$	$7.832^{+0.789}_{-0.788}$	$0.04949^{+0.00106}_{-<0.001}$	$0.235^{+0.005}_{-0.005}$	$7.833^{+0.001}_{-0.001}$	$0.04334^{+<0.001}_{-<0.001}$	[a]$0.305^{+0.065}_{-0.07}$	$7.845^{+2.55}_{-2.56}$	$0.01121^{+0.0024}_{-0.00258}$	0.47(0.005)
29	$0.285^{+0.005}_{-0.005}$	$6.785^{+0.659}_{-0.659}$	$0.09569^{+0.00165}_{-0.00165}$	$0.255^{+<0.001}_{-0.005}$	$6.776^{+<0.001}_{-0.002}$	$0.08947^{+<0.001}_{-0.00173}$	⋯	⋯	⋯	0.54(0.03)
30	$0.73^{+0.01}_{-0.01}$	$7.856^{+0.563}_{-0.563}$	$0.1295^{+0.0018}_{-0.0018}$	$0.685^{+<0.001}_{-0.025}$	$7.852^{+<0.001}_{-0.002}$	$0.1088^{+<0.001}_{-0.0039}$	[a]$0.875^{+0.075}_{-0.075}$	$7.869^{+2.27}_{-2.27}$	$0.01661^{+0.00144}_{-0.00143}$	1.4(0.045)
31	$0.86^{+0.025}_{-0.01}$	$7.791^{+0.496}_{-0.493}$	$0.1476^{+0.0042}_{-0.0017}$	$0.765^{+0.005}_{-0.005}$	$7.784^{+<0.001}_{-<0.001}$	$0.1181^{+<0.001}_{-<0.001}$	$0.765^{+0.05}_{-0.05}$	$7.784^{+2.1}_{-2.1}$	$0.0214^{+0.00142}_{-0.00142}$	1.6(0.095)
32	$1.395^{+0.035}_{-0.095}$	$7.6^{+0.412}_{-0.423}$	$0.2673^{+0.0065}_{-0.0179}$	$1.385^{+0.045}_{-0.105}$	$7.6^{+0.003}_{-0.006}$	$0.2314^{+0.0073}_{-0.0172}$	$1.52^{+0.09}_{-0.115}$	$7.607^{+1.84}_{-1.84}$	$0.04239^{+0.00257}_{-0.0033}$	2.8(0.01)
33	$0.625^{+0.01}_{-0.015}$	$8.096^{+0.431}_{-0.429}$	$0.1327^{+0.0021}_{-0.0031}$	$0.565^{+0.005}_{-0.005}$	$8.092^{+<0.001}_{-<0.001}$	$0.1086^{+<0.001}_{-0.001}$	[a]$0.78^{+0.11}_{-0.135}$	$8.107^{+2.04}_{-2.05}$	$0.02077^{+0.00298}_{-0.00364}$	1.2(0.06)
35	$1.445^{+<0.001}_{-0.075}$	$7.393^{+0.509}_{-0.518}$	$0.2845^{+<0.001}_{-0.0143}$	$1.36^{+0.03}_{-0.1}$	$7.386^{+0.003}_{-0.009}$	$0.2529^{+0.0054}_{-0.0181}$	$1.57^{+0.035}_{-0.015}$	$7.404^{+2.02}_{-2.02}$	$0.0459^{+0.00105}_{-<0.001}$	2.8(0.085)
36	$0.68^{+0.01}_{-0.01}$	$7.414^{+0.605}_{-0.609}$	$0.1738^{+0.0025}_{-0.0025}$	$0.63^{+0.015}_{-0.02}$	$7.407^{+0.003}_{-0.002}$	$0.1454^{+0.0034}_{-0.0046}$	$0.825^{+0.04}_{-0.07}$	$7.435^{+2.16}_{-2.17}$	$0.03837^{+0.00189}_{-0.0033}$	1.3(0.05)
37	$0.525^{+0.015}_{-0.01}$	$8.275^{+0.466}_{-0.463}$	$0.1166^{+0.0033}_{-0.0022}$	$0.485^{+0.01}_{-<0.001}$	$8.272^{+0.001}_{-<0.001}$	$0.09034^{+0.00184}_{-<0.001}$	[a]$0.43^{+0.055}_{-0.06}$	$8.268^{+2.17}_{-2.17}$	$0.008782^{+0.00113}_{-0.00123}$	1.0(0.04)
39	$0.71^{+0.02}_{-0.02}$	$8.35^{+0.387}_{-0.383}$	$0.1643^{+0.0046}_{-0.0046}$	$0.68^{+0.01}_{-0.005}$	$8.348^{+0.001}_{-<0.001}$	$0.1332^{+0.0019}_{-0.001}$	$0.895^{+0.06}_{-0.065}$	$8.36^{+1.91}_{-1.92}$	$0.02044^{+0.0014}_{-0.00151}$	1.4(0.03)

Notes. We have listed column densities N, excitation temperature T_{ex}, and optical depth τ calculated for the three methanol transitions from brightest to weakest.
[a] Cores for which we only had upper limits for ($<4\sigma_{rms}$). For six of the cores, the weakest transition was not detected, and we only report the brightest two transitions.

Table 7
Acetaldehyde: N and T_{ex}

Core	N (10^{12} cm^{-2})	T_{ex} (K)
4	$2.741^{+3.223}_{-1.123}$	$3.18^{+0.25}_{-0.22}$
6	$0.582^{+0.357}_{-0.175}$	$5.39^{+1.81}_{-1.02}$
9	$1.172^{+0.468}_{-0.303}$	$4.33^{+0.53}_{-0.41}$
22	$2.572^{+1.735}_{-1.987}$	$3.06^{+0.52}_{-0.13}$
30	$1.957^{+10.293}_{-1.082}$	$3.23^{+0.48}_{-0.40}$
35	$1.453^{+0.752}_{-0.432}$	$3.91^{+0.35}_{-0.43}$
Range	1.172–5.812	3.06–5.39
2	$1.219^{+0.218}_{-0.218}$	3.57
5	$2.528^{+0.327}_{-0.327}$	3.57
8	$0.814^{+0.11}_{-0.11}$	3.57
10	$1.953^{+0.218}_{-0.218}$	3.57
11	$1.012^{+0.109}_{-0.109}$	3.57
12	$1.898^{+0.218}_{-0.218}$	3.57
13	$2.393^{+0.327}_{-0.327}$	3.57
14	$1.314^{+0.218}_{-0.218}$	3.57
16	$1.287^{+0.218}_{-0.218}$	3.57
20	$0.887^{+0.11}_{-0.11}$	3.57
21	$0.793^{+0.11}_{-0.11}$	3.57
29	$0.645^{+0.11}_{-0.11}$	3.57
32	$2.970^{+0.218}_{-0.218}$	3.57
33	$1.138^{+0.218}_{-0.218}$	3.57
36	$1.243^{+0.11}_{-0.11}$	3.57
37	$1.398^{+0.11}_{-0.11}$	3.57
Range	0.65–5.81	...

Note. The table is split up into the six cores where both transitions were detected (see Figure 13) and the remaining 16 cores, in which we extrapolate the column densities from the median T_{ex} of the six cores. Note that the estimate for core 21 is from the E state, and the rest are from the brighter A state line. We quote the range of column densities for just the six cores, as well as for all 22 cores.

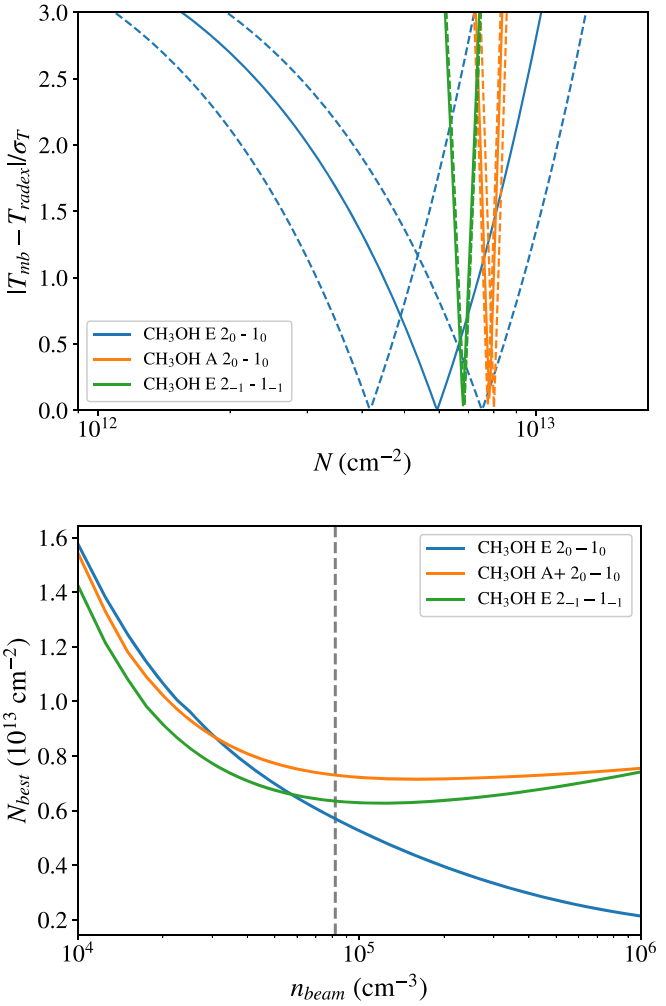

Figure 6. (Top panel) The difference in observed vs. modeled radiation temperature divided by the rms of our data ($|T_{mb} - T_{radex}|/\sigma_T$) is plotted against the column density from RADEX models for Seo15. Dashed curves represent the error as determined from grids of RADEX models run for the extrema of the errors that go into the calculation (volume density, kinetic temperature, etc.). (Bottom panel) We plot how column density changes with varying inputs of volume density for core Seo15. For the two bright CH_3OH transitions (orange and green lines), a span of 2 orders of magnitude variation in the volume density within the beam will result in only a factor of 2 variation in column density. The beam-averaged volume density for Seo15 is plotted as a gray dashed line.

where R_{eff} is the core effective radius, M is the mass of the core, σ_v is the velocity dispersion from the ammonia observations, and G is the gravitational constant. The effective radius is defined as

$$R_{eff} = \sqrt{A/\pi}, \quad (2)$$

where A is the area defined from the ammonia NH_3 (1, 1) intensity maps as described by Seo et al. (2015). The mass is calculated within the appropriate core area using the *Herschel* column density map (subtracting off background). See Section 3 for further discussion of source size and extraction from *Herschel* maps. The cores with methanol abundances $<1.0 \times 10^{-9}$ are the cores considered "gravitationally bound" by the α parameter (Figure 7, right). Cores that are less gravitationally bound have had less time to collapse and thus are considered less dynamically evolved. This result also agrees with the chemical evolution expected for methanol. Recent studies suggest that many starless cores are actually confined by external pressure, not their own gravity (Chen et al. 2019). A full virial analysis combined with radiative transfer models of methanol observations of the cores is beyond the scope of this paper and will be discussed in detail in a subsequent paper.

Abundance measurements for each core versus volume density within our beam are plotted in Figure 8. Volume density is also a potential evolutionary indicator, although it is not the sole evolutionary parameter, as cores can evolve at different rates (Shirley et al. 2005). We preface that all of the abundance plot comparisons have low correlation coefficients ($|r| < 0.26$). However, in general, there are higher $N(CH_3OH)/N(H_2)$ values at lower volume densities, and there is more scatter across volume densities at lower $N(CH_3OH)/N(H_2)$ values. We have listed in Table 8 all abundance measurements for each core, including NH_3 measurements from Seo et al. (2015). Comparing the $N(NH_3)/N(CH_3OH)$ ratio, a late-time chemical tracer, to n_{beam}, the ratio scatters toward higher abundance with increasing volume density (Figure 8).

Table 8
Abundances

Core	$N(CH_3OH)/N(H_2)$ 10^{-9}	$N(CH_3CHO)/N(H_2)$ 10^{-9}	$N(CH_3CHO)/N(CH_3OH)$	$N(NH_3)/N(H_2)$ 10^{-9}
2	$0.745^{+0.00826}_{-0.0101}$	$0.0633^{+0.0103}_{-0.0126}$	$0.0849^{+0.0138}_{-0.0169}$	1.89(0.394)
4	$0.762^{+0.0173}_{-0.0211}$	$0.139^{+0.148}_{-0.0632}$	$0.182^{+0.195}_{-0.0831}$	0.306(0.1)
5	$1.8^{+0.0161}_{-0.0197}$	$0.163^{+0.0191}_{-0.0234}$	$0.0904^{+0.0107}_{-0.013}$	0.605(0.124)
6	$1.78^{+0.0337}_{-0.0412}$	$0.0392^{+0.0219}_{-0.0131}$	$0.022^{+0.0123}_{-0.00738}$	0.941(0.192)
7	$1.01^{+0.0155}_{-0.019}$	…	…	1.6(0.245)
8	$1.13^{+0.0209}_{-0.0256}$	$0.068^{+0.00828}_{-0.0101}$	$0.06^{+0.00739}_{-0.00904}$	1.95(0.32)
9	$1.48^{+0.0259}_{-0.0317}$	$0.0743^{+0.027}_{-0.0213}$	$0.0503^{+0.0183}_{-0.0145}$	1.82(0.442)
10	$2.52^{+0.0422}_{-0.0516}$	$0.227^{+0.023}_{-0.0281}$	$0.09^{+0.00925}_{-0.0113}$	1.05(0.35)
11	$3.36^{+0.0687}_{-0.0839}$	$0.133^{+0.013}_{-0.0159}$	$0.0396^{+0.00396}_{-0.00484}$	…
12	$1.74^{+0.0221}_{-0.027}$	$0.116^{+0.0121}_{-0.0147}$	$0.0664^{+0.00698}_{-0.00853}$	1.74(0.238)
13	$2.18^{+0.0487}_{-0.0595}$	[a]$0.205^{+0.0255}_{-0.0311}$	[a]$0.094^{+0.0119}_{-0.0145}$	0.908(0.206)
14	$2.81^{+0.0613}_{-0.0749}$	[a]$0.107^{+0.0162}_{-0.0198}$	[a]$0.0383^{+0.00583}_{-0.00712}$	0.923(0.185)
15	$1.36^{+0.0425}_{-0.0519}$	…	…	1.03(0.198)
16	$1.29^{+0.0243}_{-0.0297}$	[a]$0.106^{+0.0163}_{-0.0199}$	[a]$0.0823^{+0.0128}_{-0.0156}$	1.28(0.215)
17	$0.636^{+0.0241}_{-0.0295}$	…	…	2.26(0.342)
20	$1.34^{+0.0414}_{-0.0506}$	[a]$0.0769^{+0.00859}_{-0.0105}$	[a]$0.0574^{+0.00665}_{-0.00813}$	0.699(0.247)
21	$0.916^{+0.00626}_{-0.00766}$	$0.0547^{+0.00682}_{-0.00834}$	$0.0597^{+0.00746}_{-0.00911}$	0.791(0.2)
22	$0.653^{+0.0137}_{-0.0167}$	$0.172^{+0.106}_{-0.148}$	$0.264^{+0.162}_{-0.227}$	2.27(0.429)
24	$0.525^{+0.0139}_{-0.0169}$	…	…	4.06(0.465)
26	$0.644^{+0.0216}_{-0.0264}$	…	…	1.06(0.313)
27	$0.55^{+0.00301}_{-0.00368}$	…	…	0.898(0.26)
28	$0.645^{+0.00315}_{-0.00386}$	…	…	1.38(0.353)
29	$0.857^{+0.0216}_{-0.0264}$	$0.102^{+0.0157}_{-0.0192}$	$0.119^{+0.0186}_{-0.0227}$	1.41(0.35)
30	$1.24^{+0.0179}_{-0.0219}$	$0.171^{+0.819}_{-0.105}$	$0.138^{+0.661}_{-0.085}$	1.77(0.328)
31	$1.24^{+0.0329}_{-0.0402}$	…	…	0.862(0.14)
32	$1.72^{+0.00282}_{-0.00344}$	$0.184^{+0.0123}_{-0.015}$	$0.107^{+0.00713}_{-0.00871}$	0.471(0.129)
33	$0.701^{+0.0161}_{-0.0196}$	$0.0671^{+0.0117}_{-0.0143}$	$0.0957^{+0.0168}_{-0.0205}$	3.8(0.53)
35	$2.48^{+0.0342}_{-0.0418}$	$0.129^{+0.0606}_{-0.0425}$	$0.0518^{+0.0244}_{-0.0171}$	0.736(0.233)
36	$1.44^{+0.0249}_{-0.0305}$	$0.136^{+0.0109}_{-0.0133}$	$0.0949^{+0.00774}_{-0.00946}$	0.822(0.308)
37	$0.622^{+0.0112}_{-0.0137}$	$0.0861^{+0.0061}_{-0.00745}$	$0.138^{+0.0101}_{-0.0124}$	3.27(0.446)
39	$0.644^{+0.00632}_{-0.00773}$	…	…	2.35(0.326)

Notes. The methanol column density used to calculate abundances is the total (A+E state) value reported in the 11th column of Table 6. The $N(NH_3)/N(H_2)$ from the abundance maps is provided by Seo et al. (2015), which we use to calculate what the median ratio would be within our methanol beam size (standard deviation in parentheses).
[a] Derived from upper limit CH_3CHO measurements.

4.2. CH_3OH Spatial Distribution

We mapped seven $15' \times 15'$ regions within the Taurus filament in the 96.7 GHz transitions of methanol, focusing on the regions where our starless cores reside. These seven maps are named based on the Barnard region they lie in, i.e., B7, B10, B211, B213-1, B213-2, B216, and B218. In Figure 5, we overlay the CH_3OH integrated intensity map contours on an extinction map from Schmalzl et al. (2010) in steps of 0.2 K km s^{-1} ($\sim 2\sigma$ detection). The uniformly generated and Gaussian smoothed extinction map, at similar resolution as our CH_3OH beam ($\sim 1'$), was generated from near-infrared photometry (*JHK*$_s$ bands) of point sources throughout the Taurus L1495 filaments. We detected methanol emission at A_V as low as ~ 3 mag (noise at $\sigma \sim 0.5$ mag). In Table 9 we quote the lowest extinction and H_2 column density values where methanol is detected at our $\sim 2\sigma$ level in each region.

For every region except B10, the integrated intensity maps were made within a velocity range of 3.19–8.03 km s^{-1}, where each channel was spaced by 0.12 km s^{-1}. In the case of B10, the range was from 5.09 to 7.51 km s^{-1} spaced by 0.06 km s^{-1}.

Table 9
Lowest Level Extinction

OTF Mapped Region	A_V (mag)	N_{H_2} (10^{21} cm^{-2})
B7	11	6
B10	5	4
B211	4	3
B213[a]	5	3
B216	4	3
B218	3	2

Notes. The values reported are the A_V and N_{H_2} for which CH_3OH emission is detected at the 2σ level from OTF maps.
[a] Including both B213-1 and B213-2 maps.

By using this cutoff, we focused only on the single brightest methanol transition, CH_3OH A 2_0–1_0. Regions denoted as less evolved, i.e., B211 and B10 in particular, show significant extended methanol emission (Figures 5 and 9) in addition to having higher methanol abundances from the single-pointing

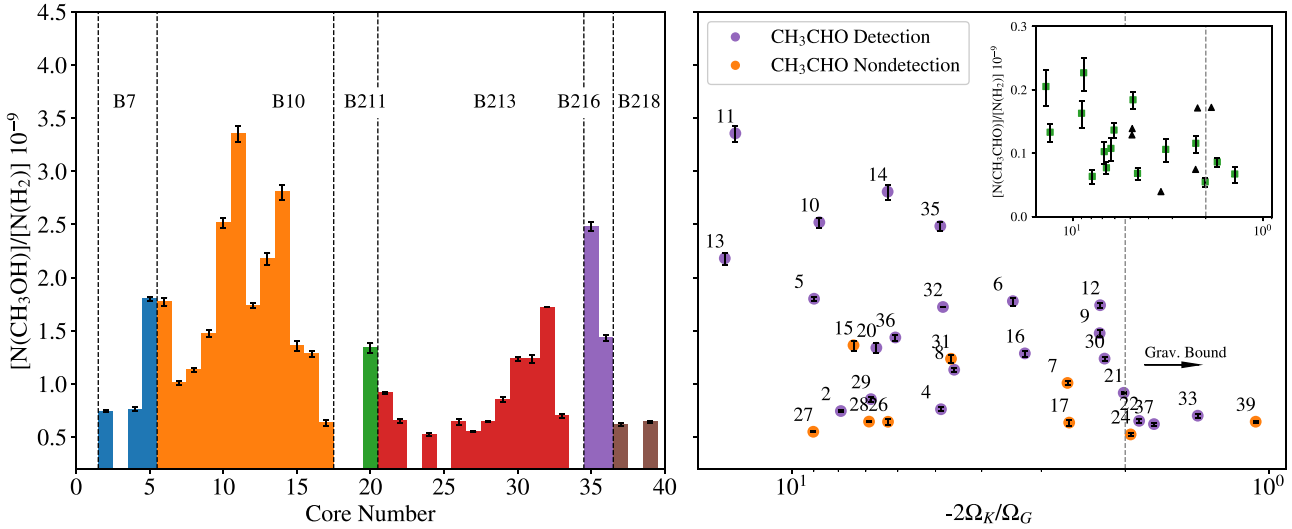

Figure 7. (Left panel) Plot of methanol abundance vs. core, color-coded for each Barnard region that the cores are located in. The less evolved regions (determined by the lack of protostellar sources), i.e., B10, B211, and B216, have higher methanol abundances compared to the other more evolved regions. (Right panel) Abundances vs. virial ratio, $\alpha = 2\Omega_K/\Omega_G = 5\sigma^2 R/GM$. In orange, we denote in which cores CH_3CHO was not detected. In the inset, black triangles represent the six cores for which two transitions of CH_3CHO were detected and whose median T_{ex} value was used to calculate the column density for the remaining cores. Error bars for these six cores have been removed due to large dispersion (see Figure 13). Note that the x-axis increases toward the left.

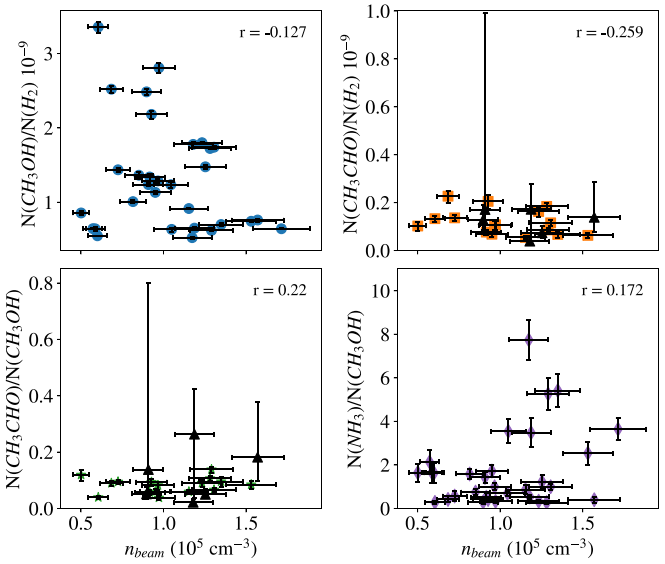

Figure 8. Plots of abundance and abundance ratios vs. volume density, n_{beam}. The top left panel plots CH_3OH abundance with regard to H_2 as blue circles, the top right plots CH_3CHO with regard to H_2 as orange squares, the bottom left plots CH_3CHO with regard to CH_3OH as green stars, and the bottom right plots NH_3 with regard to CH_3OH as purple diamonds (NH_3 values from Seo et al. 2015). The black triangles symbolize the cores we detected both CH_3CHO transitions in, as in Figure 7. The core with the largest error bar is Seo30, whose column density was poorly constrained by the CTEX method (see Figure 13). We report the Spearman rank correlation coefficient in the top right corner of each panel.

observations (Figure 7). Even though our OTF integrated intensity maps are at modest angular resolution, we see indications of chemical differentiation. This can be clearly seen for Seo9 in the B10 region, which is one of the densest of the cores; i.e., the ∼7 km s^{-1} methanol velocity component only slightly overlaps the Seo9 peak position (see Figure 9).

We created a methanol abundance map of the "less evolved" (i.e., no signs of protostars) B211 region. Gaussian line profiles were fit using CLASS at each point in the map, which is convolved to a finer resolution of 75″ (compared to 81″ in Figures 5 and 9). We chose positions in our grid with integrated intensities of the brightest (CH_3OH A^+ 2_0–1_0) line that lie above the 5σ rms level and ran these points through a RADEX grid that calculates column densities and abundances (compared to H_2 from the *Herschel* maps) for CH_3OH. The B211 region was the only region with enough points above 5σ to create a reliable, spatially connected abundance map (see Figure 10). In Figure 11, we present three of our regridded maps of peak brightness (T_{mb}), A_V, and abundance. The peaks in the abundance map do not correspond to where core Seo20 is located; i.e., we find higher abundances along the filament than for the starless core itself. Extended emission in the filaments is also brighter than what was detected toward the NH_3-peak core positions by an order of magnitude in most other regions. This anticorrelation between bright methanol and dust emission toward core Seo20 is a clear sign of depletion, even given our modest spatial resolution, seen on larger filament-size scales.

Putting together the trends discussed, we conclude that chemical differentiation of methanol due to depletion in the central regions of cores is occurring. As suggested by the chemical desorption models of Vasyunin et al. (2017), methanol should preferentially be found in a shell around the dense central regions, where visual extinctions are large enough to screen interstellar UV photons (⩾10 mag) and volume densities are around a few $\times 10^4$ cm^{-3}. In fact, higher-resolution observations of methanol toward more chemically evolved dense cores (L1498, L1517B, L1544; Tafalla et al. 2006; Bizzocchi et al. 2014) have already revealed such ringlike structures in methanol emission.

4.2.1. Multiple Velocity Peaks and Large-scale Motions

There are three cores (∼10% of the sample) that are spatially nearby (Seo17, Seo20, and Seo21) and have shown clear evidence of multiple velocity components in our single-pointing observations (see Figure 2). Multiple velocity components have been seen in other molecular lines in this same region, i.e., $C^{18}O(1-0)$ and $N_2H^+(1-0)$ (Hacar et al. 2013). They found two previously

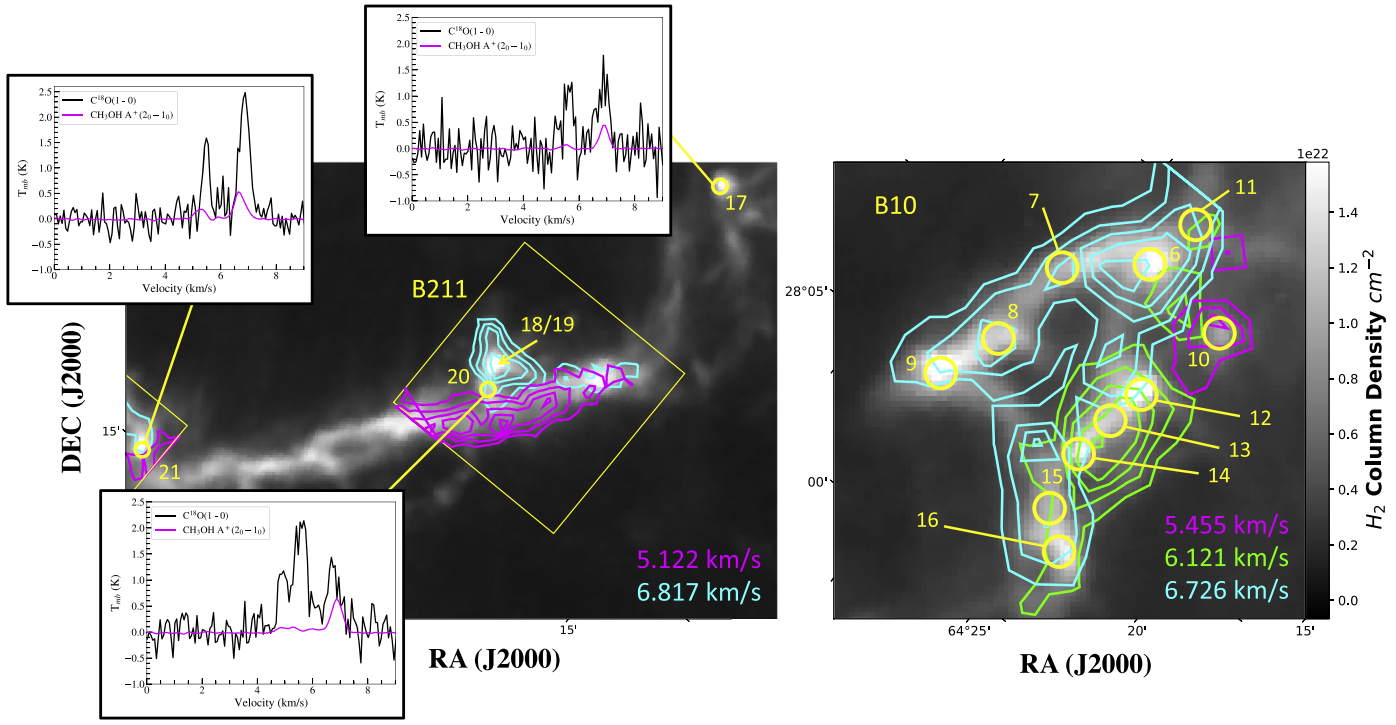

Figure 9. Maps (gray scale is H_2 column density) of the (left) B211 and (right) B10 regions illustrating the complex velocity structure of methanol emission. On the left, three panels of spectra are shown, with $C^{18}O(1-0)$ molecular observations from the IRAM 30 m telescope in black (Hacar et al. 2013). For comparison, we include the positions of the methanol peaks that show similar velocity structure as $C^{18}O(1-0)$. We shifted the bright A^+ to the center to show how the v_{LSR} values compare, showing some misalignment perhaps due to gas motions within the filament. The yellow circles represent the cores targeted in those regions. In B211, we also note with a yellow arrow where cores Seo18 and Seo19 lie from Seo et al. (2015; these were not targeted for APS measurements due to overlapping beams). For both regions, main beam temperature contours (in steps of 0.2 K starting at 0.2 K) were created in cyan at a velocity of ∼7 km s^{-1}, lime at a velocity of ∼6 km s^{-1}, and magenta at a velocity of ∼5 km s^{-1}.

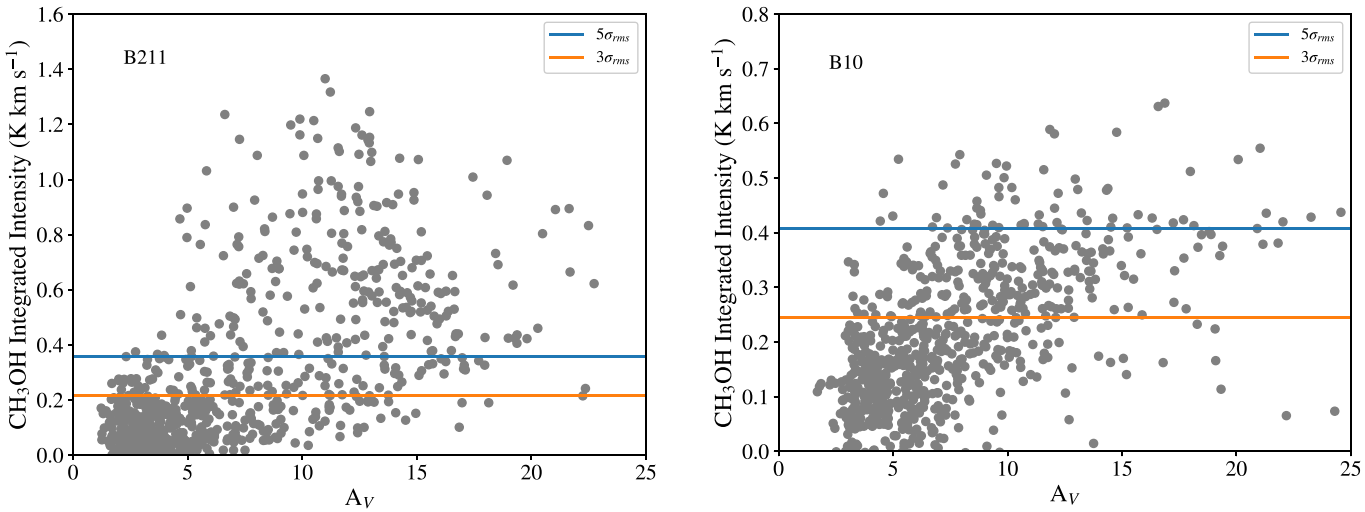

Figure 10. Brightest methanol peak intensity vs. A_V for the (left) B211 and (right) B10 regions in Taurus. Here B211 is the only region used to create a reliable, contiguous map, created from integrated intensities that are $\geqslant 5\sigma$.

known velocity components (near 5.3 and 6.7 km s^{-1}), and we find similar components at roughly the same v_{LSR}. Specifically, in core Seo20, each component peaks at 5.1 and 6.9 km s^{-1}, respectively. Multiple velocity components for methanol were seen clearly in not just the single pointings but in the OTF maps. In the B211 region, a clear spatial separation of emission is found; i.e., in the ∼5 km s^{-1} velocity channel, we see methanol tracing the filament, and in the ∼7 km s^{-1} velocity channel, methanol is centered around the starless cores Seo18/19, which were not included in our single-pointing survey due to overlapping beams (Figure 9). Observations in B10 also showed clear spatial separation of velocity components, telling us that the methanol in these starless cores is not all coming from the same velocity structure but rather from multiple velocity channels at ∼5, ∼6, and ∼7 km s^{-1} (Figure 9).

Perhaps it is not surprising that we observe multiple velocity components. In TMC-1, it is well known that two or more velocity components exist and that the line profile of CH_3OH is significantly broader than those of other molecules (Soma et al. 2015). Also, 17 dense cores in Tang et al. (2018) were found to

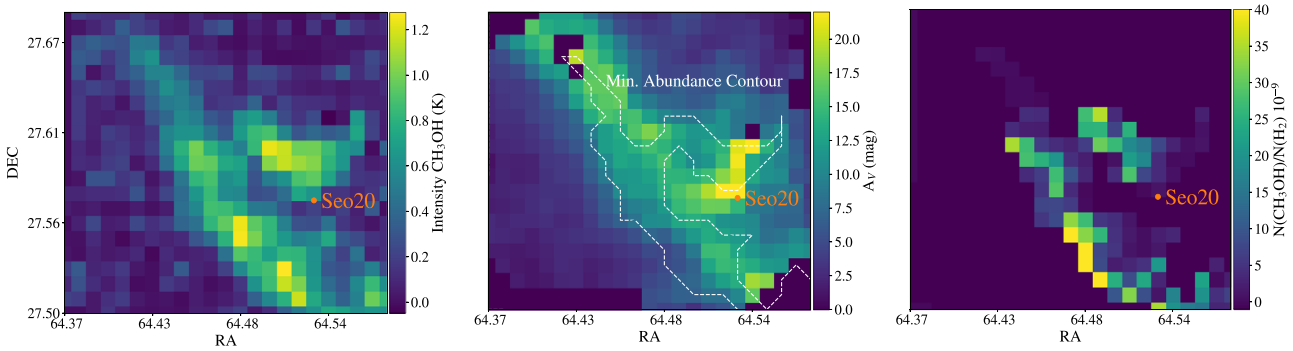

Figure 11. Regridded CH_3OH brightness (T_{mb}), A_V, and abundance maps, each convolved to 75″ resolution, for the B211 region of Taurus (left to right). The abundance map was created from points that were at least 5σ detections in intensity.

have multiple velocity peaks in ^{12}CO, and in the case of Seo21 (which they mapped), the peaks occur at 5.40 and 7.49 km s^{-1}, which is close to what we observe in CH_3OH. The ∼5 km s^{-1} velocity peak corresponds to that of the extended filament emission that Hacar et al. (2013) observed in $C^{18}O$. Thus, CH_3OH is tracing multiple parts of the cloud/filament along some lines of sight.

In addition to the spatial separations in velocity, the CH_3OH line widths have revealed a combination of unresolved bulk motions (gradients or flows) and supersonic turbulence. Using just the two brightest transition lines (A^+ 2_0–1_0 and E 2_{-1}–1_{-1}) for comparison, we found that the line widths of our CH_3OH lines were broader, at an average of ∼0.45 km s^{-1} wide, than those of NH_3 observed by Seo et al. (2015; top panel of Figure 12). The ratio of thermal to nonthermal support was also smaller, on average, for CH_3OH than for NH_3, telling us that the methanol has a larger nonthermal contribution (middle panel of Figure 12). Methanol emission is optically thin (Section 4.1); therefore, optical depth is not the culprit for the wider line widths. The nonthermal line-width difference between NH_3 and CH_3OH could certainly arise from their difference in sampling different densities of gas and therefore different large-scale motions along the line of sight.

In ∼30% of the cores, there is evidence for non-Gaussian line asymmetries, or "wings;" for example, from its spectrum core, Seo12 appears to have a redshifted wing, whereas Seo16 has a blueshifted wing (Figure 2). Regardless, for our line analysis (Gaussian fitting), we were only concerned with comparing the central velocity component (∼7 km s^{-1}) at the v_{LSR} of the cores. Line asymmetries most likely represent a mixture of large-scale motions from within the core, as well as the surrounding material that we detected within our large (62.″3) beam.

4.3. CH_3CHO Column Densities

We detected acetaldehyde in 22 of the 31 cores, where 18 of the 22 were observed with at least 4σ confidence at rms values of ∼4–6 mK (Figure 3 and Table 4). Starless cores Seo11 and Seo20 are unique in that we detected the A but not the E transition state. Additionally, for core Seo21, we detected the E transition but not the A transition. In all other cases, because both the A and E lines were in the bandpass, and since they have similar upper energy levels ($E_u/k = 13.935$ K for CH_3CHO E and $E_u/k = 13.838$ K for CH_3CHO A), we could confirm CH_3CHO with a single spectrum. The cores with the highest main beam temperature were Seo32, Seo35, Seo9, Seo5, and Seo4 (from brightest to weakest).

We found that six of the 22 cores detected in the $5_{(0,5)}$–$4_{(0,4)}$ transition were also detectable in the 84 GHz CH_3CHO A $2_{(1,2)}$–$1_{(0,1)}$ transition, after integrating down to rms values of ∼3–4 mK (Table 3 and Figure 4). Since CH_3CHO has no calculated collisional rate coefficients, RADEX calculations are not possible. We used the CTEX method, which required at least two transitions with different E_u/k values to simultaneously constrain T_{ex} and the column density, N (see Equation (80) of Mangum & Shirley 2015). Both the $5_{(0,5)}$–$4_{(0,4)}$ and $2_{(1,2)}$–$1_{(0,1)}$ transitions were used to calculate N and T_{ex} for the six cores we detected both transitions in. The ranges for the six cores are $N = (1.2\text{–}5.8) \times 10^{12}$ cm^{-2} and $T_{ex} = 3.1\text{–}5.4$ K (Figure 13 and Table 7).

We extrapolated our results from CTEX in order to estimate the column densities for the remaining 16 cores where only the CH_3CHO $5_{(0,5)}$–$4_{(0,4)}$ transition was detected. We used the median excitation temperature of the six cores, $T_{ex} = 3.57$ K, and calculated the column density at that temperature. The total range of column densities for all 22 cores is (0.65–5.8) × 10^{12} cm^{-2} (Table 7).

4.3.1. CH_3CHO Abundance Trends

Previous studies have searched for acetaldehyde in only a handful of dense cores, including detections toward L183, TMC-1, CB17, L1689B, and L1544 (Turner et al. 1999; Bacmann et al. 2012; Jiménez-Serra et al. 2016). Vastel et al. (2014) calculated a CH_3CHO column density of 5.0 × 10^{11} for L1544; however, they assumed T_{ex} of 17 K. At a more realistic T_{ex} of 5 K, Jiménez-Serra et al. (2016) reported a column density of 1.2 × 10^{12} cm^{-2} at the center of L1544. The CH_3CHO column density at T_{ex} of 5 K for another very dense core, L1689B, for the E state 5–4 transitions was found to be (9.12 ± 0.92) × 10^{12} cm^{-2}, and for the A state 5–4 transition, (8.26 ± 0.84) × 10^{12} cm^{-2} (Bacmann et al. 2012). Our results suggest that our cores lie in between these core estimates.

Acetaldehyde abundances compared to methanol, [CH_3CHO]/[CH_3OH], range from 0.02 to 0.26 for the Taurus cores presented here. We note that many of the nondetections of CH_3CHO come from the B213 region, the same region where we detected multiple velocity components and lower abundances of CH_3OH ($\lesssim 1.5 \times 10^{-9}$). Additionally, B213 is one of the most evolved regions with multiple embedded protostars. In the right panel of Figure 7, we show that cores with nondetections of CH_3CHO all have methanol abundances $<1.5 \times 10^{-9}$ and that as abundances

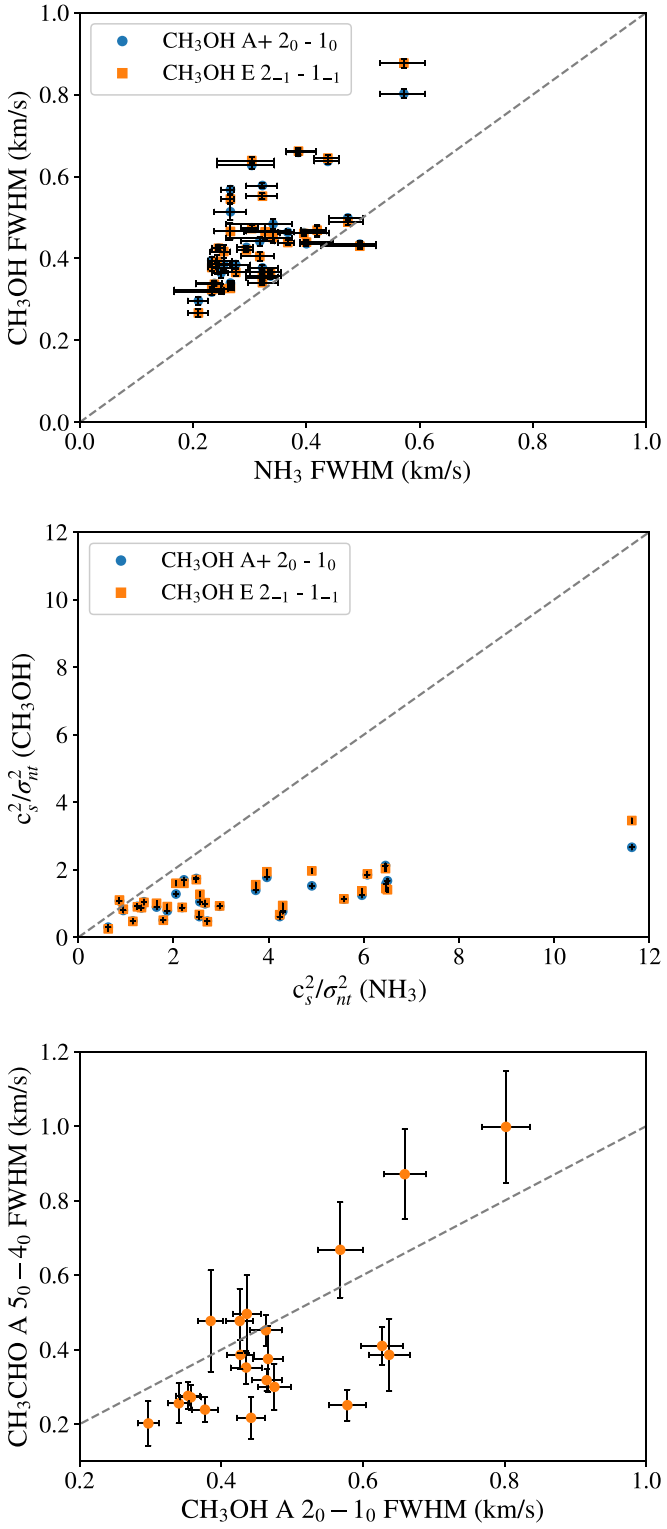

Figure 12. (Top panel) Observed methanol line widths vs. ammonia line widths from Seo et al. (2015). (Middle panel) Plot of the ratio of thermal support to nonthermal support for methanol vs. ammonia. (Bottom panel) We compare line widths of methanol and acetaldehyde, finding a median line-width ratio (CH_3CHO/CH_3OH) of 0.62.

(with regard to H_2) drop, the virial parameter is larger (i.e., the core is more evolved). As cores evolve, the abundance of both CH_3OH and CH_3CHO declines, suggesting that the formation processes for these two molecules are linked.

4.4. CH_3CHO Line Widths

In general, the line widths of the CH_3CHO A transition are narrower than those of methanol, with the average FWHM ∼0.23 km s^{-1} wide (bottom panel of Figure 12). The narrower line widths indicate that the acetaldehyde is likely not tracing the full extent of A_V that is being traced by the methanol within the beam. The measured v_{LSR} values of CH_3CHO and CH_3OH are (on average) within ∼0.1 km s^{-1} of each other. Soma et al. (2018) also found narrower line widths for CH_3CHO versus CH_3OH in TMC-1. Unfortunately, the acetaldehyde emission is weak, which made it unfeasible to map the emission in a reasonable amount of time.

5. Discussion

The main conclusion of this paper is that methanol and acetaldehyde are easily observable in the gas phase toward a large sample of starless and prestellar cores with a range of densities and ages in the Taurus molecular cloud. Both CH_3OH and CH_3CHO are prevalent (100% and 70% detection rates, respectively) with high gas-phase abundances ($\sim10^{-10}$ to 10^{-9} with regard to H_2). Given typical phase lifetimes of prestellar cores with densities $\sim10^5$ cm^{-3} of a few $\times10^5$ yr (see Figure 7 of André et al. 2014), at a minimum, COM formation predates the formation of a first hydrostatic core by many hundreds of thousands of years. Thus, with subsequent COM depletion in the central regions during the evolution of prestellar cores into first hydrostatic cores, our results suggest that protoplanetary disks will be seeded with COMs that have formed during the prestellar phase. Here we discuss the link between methanol and acetaldehyde, addressing how they might chemically coevolve.

From our OTF maps, we detect CH_3OH down to an A_V of ∼3 mag, roughly where CO ice begins to form. The formation of CO ice begins in the gas phase, during the so-called catastrophic CO freeze-out stage, when it accretes onto layers of water ice that has already formed, resulting in a CO-rich apolar ice coating (Tielens et al. 1991; Pontoppidan 2006; Öberg et al. 2011). From both astrochemical modeling and observations, CO freeze-out in cold cores has been shown to occur at densities similar to starless core densities, i.e., a few 10^5 cm^{-3} (Jørgensen et al. 2005; Lippok et al. 2013). Methanol formation is believed to follow this freeze-out process, since CO freeze-out is a prerequisite for CH_3OH ice formation without energetic radiation (Cuppen et al. 2009). According to chemical desorption models, radicals are then desorbed off the ice and dust grains, which react in the gas phase to form more complex organics, like CH_3CHO (Vasyunin & Herbst 2013; Vastel et al. 2014). Observations from Vastel et al. (2014) support this idea, finding that more complex organics, in addition to precursor methanol, are likely coming from an outer shell (∼8000 au for L1544) in a region where the ices are desorbed through nonthermal processes.

There are few possible gas-phase reactions that will form CH_3CHO in cold prestellar core environments. In one scenario, CH_3CHO is formed in the gas phase by oxidation of the ethyl radical ($C_2H_5 + O \rightarrow CH_3CHO + H$), as described by Charnley (2004). This reaction, however, is not likely in cold cores due to the negligible reactive desorption probability of more complex radicals; i.e., C_2H_5 is predicted to have a very low reactive desorption probability (Minissale et al. 2016). The most likely gas-phase reaction occurs between the methylidyne radical, CH, and methanol, CH_3OH, to form CH_3CHO, along with a hydrogen atom (Johnson et al. 2000). This reaction

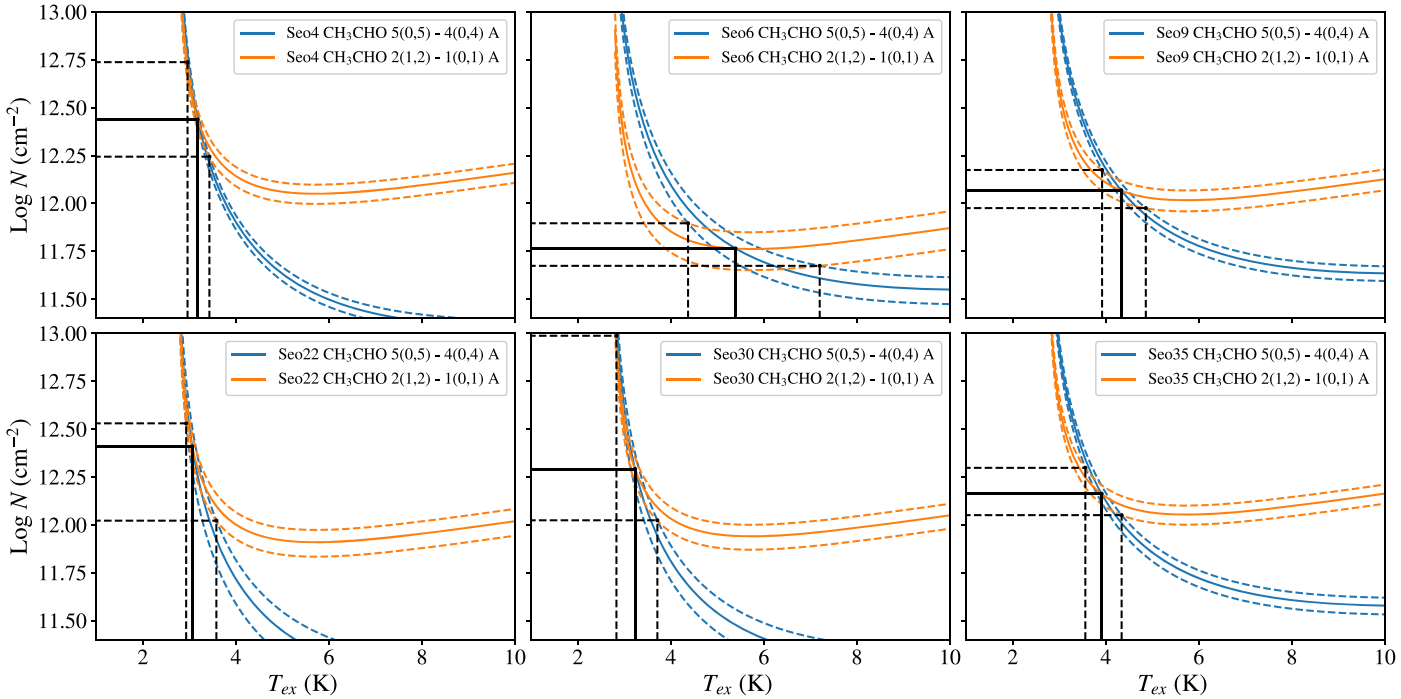

Figure 13. Log column density vs. excitation temperature calculated for two transitions of CH_3CHO using the CTEX method. The curves for each CH_3CHO transition were calculated given the observed integrated intensities and are plotted for all six of the cores for which both transitions of CH_3CHO were detected. Intersecting values are recorded in Table 7.

requires methanol to have already been chemically desorbed into the gas phase. The chemical link between CH_3OH and CH_3CHO is supported by the models of Vasyunin et al. (2017), which show a strong similarity in the radial abundance profiles of both species (see their Figure 8).

From our results, there is no significant evolutionary correlation between the abundance of CH_3CHO with respect to H_2 or CH_3CHO with respect CH_3OH with volume density (Figure 8). Furthermore, abundance trends in the range of scatter observed for CH_3OH are not observed for CH_3CHO; there is similar scatter in the CH_3CHO abundance and abundance ratios across the average volume densities probed. One reason for this may be that theoretical models of chemical desorption predict that there should be an enhancement of more complex organics, such as acetaldehyde, at both early and late times of the core's chemical evolution (Figure 7 in Vasyunin et al. 2017). Obtaining central densities for the cores may reduce this scatter, since our beam-averaged volume density measurements only probe the global properties with a limited range (factor of 4 in density).

We find that cores with lower methanol abundances are less likely to be detected in CH_3CHO. All but two of the CH_3CHO nondetections are below the median methanol abundance (Figure 7). The same trend with virial parameter for both CH_3OH and CH_3CHO is also found, that cores with smaller virial parameters (more evolved) have lower abundances (Figure 7). When we plot the column density of CH_3OH versus CH_3CHO (Figure 14), we find a weak but positive correlation ($r = 0.54$). These trends suggests that the CH + CH_3OH reaction is important for the gas-phase production of CH_3CHO in starless and prestellar cores. Still, with significant scatter in these trends, there may be other factors (i.e., beam filling fraction) affecting the relative abundances of CH_3OH and CH_3CHO that should be addressed in future high-resolution studies. Since we are still limited by our single-pointed observations, we cannot say whether strong chemical differentiation is occurring within our beam, although it seems highly likely. Obtaining higher spatial resolution maps of both species is needed to test against calculated radial profiles, spatial morphologies, and spatial scales at the core level.

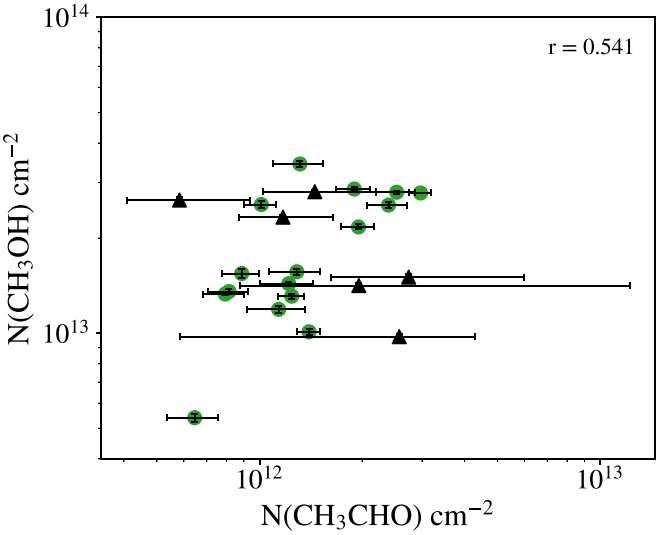

Figure 14. Column density of CH_3OH vs. CH_3CHO for the 22 cores for which CH_3CHO was detected. The black triangles symbolize the cores we detected both CH_3CHO transitions in, as in Figure 7. The Spearman rank correlation coefficient is presented in the upper right corner.

6. Summary

We found a prevalence of the organic molecules methanol (100% detection rate) and acetaldehyde (70% detection rate) toward a sample of 31 NH_3-identified starless and prestellar

cores within the L1495-B218 filament in the Taurus molecular cloud. Our systematic survey shows that COMs, specifically methanol and acetaldehyde, that are important in prebiotic chemistry are forming early and often in the starless and prestellar stages at least hundreds of thousands of years prior to the formation of protostars and planets. We have calculated the column density, excitation temperature, and abundance of CH_3OH and CH_3CHO for each core, comparing to physical properties, and we present maps of the distribution of methanol.

In all 31 cores, we detected methanol, with total column densities in the range $(0.42–3.4) \times 10^{13}$ cm^{-2} and excitation temperatures ranging from 6.79 to 8.66 K (from the brightest transition). Additionally, in 22 of the 31 cores, acetaldehyde was detected with column densities in the range $(0.65–5.81) \times 10^{12}$ cm^{-2}, with a median excitation temperature of 3.57 K. The total abundance of methanol spans $(0.53–3.36) \times 10^{-9}$, while the abundance of detected acetaldehyde spans $(0.6–3.9) \times 10^{-10}$ in the cores. Large-scale motions are evident from asymmetric CH_3OH line profiles toward some cores. Multiple velocity components were seen in both the pointed observations and the OTF mapping of methanol that match well with the previously detected velocity coherent filament traced by $C^{18}O$ 1 −0. We find that gas-phase methanol is an early-time tracer and was detected down to A_V as low as ∼3 mag. Analyses of the methanol observations are consistent with depletion in denser cores. There is evidence of a weak positive correlation between the abundances of methanol and acetaldehyde; however, the chemical connection between these two molecules in prestellar cores has yet to be observationally supported by higher spatial resolution maps.

We would like to thank Youngmin Seo for his frequent assistance and the ARO 12 m telescope operators (Michael Begam, Kevin Bays, Robert Thompson, and Clayton Kyle) who made these observations possible. We also thank our anonymous referee for constructive comments. S.S. is supported by National Science Foundation Graduate Research Fellowship (NSF GRF) grant DGE-1143953. Y.S. and S.S. were also supported in part by NSF grant AST-1410190.

Software: Astropy (Astropy Collaboration et al. 2013, 2018), NumPy (van der Walt et al. 2011), SciPy (Jones et al. 2001), Matplotlib (Hunter 2007), Ds9 (Joye & Mandel 2003), GILDAS CLASS (Pety 2005; Gildas Team 2013), RADEX (van der Tak et al. 2007).

ORCID iDs

Samantha Scibelli https://orcid.org/0000-0002-9485-4394

References

Aikawa, Y., Wakelam, V., Garrod, R. T., et al. 2008, ApJ, 674, 984
Allamandola, L. J., Sandford, S. A., & Valero, G. J. 1988, Icar, 76, 225
André, P., Di Francesco, J., Ward-Thompson, D., et al. 2014, in Protostars and Planets VI, ed. H. Beuther et al. (Tucson, AZ: Univ. Arizona Press), 27
Astropy Collaboration, Price-Whelan, A. M., Sipőcz, B. M., et al. 2018, AJ, 156, 123
Astropy Collaboration, Robitaille, T. P., Tollerud, E. J., et al. 2013, A&A, 558, A33
Bacmann, A., & Faure, A. 2016, A&A, 587, A130
Bacmann, A., Taquet, V., Faure, A., Kahane, C., & Ceccarelli, C. 2012, A&A, 541, L12
Balucani, N., Ceccarelli, C., & Taquet, V. 2015, MNRAS, 449, L16
Benson, P. J., & Myers, P. C. 1989, ApJS, 71, 89
Bergin, E. A., & Tafalla, M. 2007, ARA&A, 45, 339
Bernstein, M. P., Dworkin, J. P., Sandford, S. A., et al. 2002, Natur, 416, 401
Bernstein, M. P., Sandford, S. A., Allamandola, L. J., et al. 1995, ApJ, 454, 327
Bieging, J. H., & Peters, W. L. 2011, ApJS, 196, 18
Bizzocchi, L., Caselli, P., Spezzano, S., & Leonardo, E. 2014, A&A, 569, A27
Caselli, P., Walmsley, C. M., Zucconi, A., et al. 2002, ApJ, 565, 344
Charnley, S. B. 2004, AdSpR, 33, 23
Charnley, S. B., & Tielens, A. G. G. M. 1992, in IAU Symp. 150, Astrochemistry of Cosmic Phenomena, ed. P. D. Singh (Dordrecht: Kluwer Academic), 317
Chen, H. H.-H., Pineda, J. E., Goodman, A. A., et al. 2019, ApJ, 877, 93
Chuang, K.-J., Fedoseev, G., Qasim, D., et al. 2017, MNRAS, 467, 2552
Chuang, K.-J., Fedoseev, G., Qasim, D., et al. 2018, ApJ, 853, 102
Cuppen, H. M., van Dishoeck, E. F., Herbst, E., et al. 2009, A&A, 508, 275
de Marcellus, P., Bertrand, M., Nuevo, M., et al. 2011, AsBio, 11, 847
Dulieu, F., Nguyen, T., Congiu, E., et al. 2019, MNRAS, 484, L119
Dworkin, J. P., Deamer, D. W., Sandford, S. A., et al. 2001, PNAS, 98, 815
Evans, N. J., II, Rawlings, J. M. C., Shirley, Y. L., & Mundy, L. G. 2001, ApJ, 557, 193
Fedoseev, G., Chuang, K.-J., Ioppolo, S., et al. 2017, ApJ, 842, 52
Geppert, W. D., Hamberg, M., Thomas, R. D., et al. 2006, FaDi, 133, 177
Gildas Team 2013, GILDAS: Grenoble Image and Line Data Analysis Software, Version jul16a, Astrophysics Source Code Library, ascl:1305.010
Hacar, A., Tafalla, M., Kauffmann, J., & Kovács, A. 2013, A&A, 554, A55
Harju, J., Pineda, J. E., Vasyunin, A. I., et al. 2019, arXiv:1903.11298
Herbst, E., & van Dishoeck, E. F. 2009, ARA&A, 47, 427
Hunter, J. D. 2007, CSE, 9, 90
Jiménez-Serra, I., Vasyunin, A. I., Caselli, P., et al. 2016, ApJL, 830, L6
Johnson, D. G., Blitz, M. A., & Seakins, P. W. 2000, PCCP, 2, 2549
Jones, E., Oliphant, E., Peterson, P., et al. 2001, SciPy: Open Source Scientific Tools for Python, Version 0.19.0, http://www.scipy.org/
Jørgensen, J. K., Schöier, F. L., & van Dishoeck, E. F. 2005, A&A, 435, 177
Joye, W. A., & Mandel, E. 2003, in ASP Conf. Ser. 295, Astronomical Data Analysis Software and Systems XII, ed. H. E. Payne, R. I. Jedrzejewski, & R. N. Hook (San Francisco, CA: ASP), 489
Kirk, J. M., Ward-Thompson, D., Palmeirim, P., et al. 2013, MNRAS, 432, 1424
Lippok, N., Launhardt, R., Semenov, D., et al. 2013, A&A, 560, A41
Mangum, J. G., & Shirley, Y. L. 2015, PASP, 127, 266
Marsh, K. A., Kirk, J. M., André, P., et al. 2016, MNRAS, 459, 342
Materese, C. K., Nuevo, M., Bera, P. P., et al. 2013, AsBio, 13, 948
Minissale, M., Dulieu, F., Cazaux, S., & Hocuk, S. 2016, A&A, 585, A24
Modica, P., Martins, Z., Meinert, C., et al. 2018, ApJ, 865, 41
Nuevo, M., Cooper, G., & Sandford, S. A. 2018, NatCo, 9, 5276
Oba, Y., Tomaru, T., Lamberts, T., et al. 2018, NatAs, 2, 228
Öberg, K. I., Boogert, A. C. A., Pontoppidan, K. M., et al. 2011, ApJ, 740, 109
Öberg, K. I., van Dishoeck, E. F., Linnartz, H., et al. 2010, ApJ, 718, 832
Palmeirim, P., André, P., Kirk, J., et al. 2013, A&A, 550, A38
Pety, J. 2005, in SF2A-2005: Semaine De L'Astrophysique Francaise, ed. F. Casoli (Les Ulis: EDP Sciences), 721
Pontoppidan, K. M. 2006, A&A, 453, L47
Punanova, A., Caselli, P., Feng, S., et al. 2018, ApJ, 855, 112
Schlafly, E. F., Green, G., Finkbeiner, D. P., et al. 2014, ApJ, 786, 29
Schmalzl, M., Kainulainen, J., Quanz, S. P., et al. 2010, ApJ, 725, 1327
Seo, Y. M., Shirley, Y. L., Goldsmith, P., et al. 2015, ApJ, 805, 185
Shirley, Y. L. 2015, PASP, 127, 299
Shirley, Y. L., Huard, T. L., Pontoppidan, K. M., et al. 2011, ApJ, 728, 143
Shirley, Y. L., Nordhaus, M. K., Grcevich, J. M., et al. 2005, ApJ, 632, 982
Soma, T., Sakai, N., Watanabe, Y., & Yamamoto, S. 2015, ApJ, 802, 74
Soma, T., Sakai, N., Watanabe, Y., et al. 2018, ApJ, 854, 116
Tafalla, M., Santiago-García, J., Myers, P. C., et al. 2006, A&A, 455, 577
Tang, M., Liu, T., Qin, S.-L., et al. 2018, ApJ, 856, 141
Tielens, A. G. G. M., Tokunaga, A. T., Geballe, T. R., et al. 1991, ApJ, 381, 181
Tokuda, K., Tachihara, K., Saigo, K., et al. 2019, PASJ, 71, 73
Turner, B. E., Terzieva, R., & Herbst, E. 1999, ApJ, 518, 699
van der Tak, F. F. S., Black, J. H., Schöier, F. L., et al. 2007, A&A, 468, 627
van der Walt, S., Colbert, S. C., & Varoquaux, G. 2011, CSE, 13, 22
Vastel, C., Ceccarelli, C., Lefloch, B., et al. 2014, ApJL, 795, L2
Vasyunin, A. I., Caselli, P., Dulieu, F., & Jiménez-Serra, I. 2017, ApJ, 842, 33
Vasyunin, A. I., & Herbst, E. 2013, ApJ, 769, 34
Ward-Thompson, D., Scott, P. F., Hills, R. E., et al. 1994, MNRAS, 268, 276
Watanabe, N., & Kouchi, A. 2002, ApJL, 571, L173